



Chen, G., Zang, B., & Azarpeyvand, M. (2023). Numerical Investigation on Aerodynamic Noise of Flow past a Cylinder with Different Spanwise Lengths. *Physics of Fluids*, 35(3), [035128]. <https://doi.org/10.1063/5.0139731>

Peer reviewed version

Link to published version (if available):  
[10.1063/5.0139731](https://doi.org/10.1063/5.0139731)

[Link to publication record in Explore Bristol Research](#)  
PDF-document

This is the accepted author manuscript (AAM). The final published version (version of record) is available online via American Institute of Physics at <https://doi.org/10.1063/5.0139731>. Please refer to any applicable terms of use of the publisher.

## University of Bristol - Explore Bristol Research

### General rights

This document is made available in accordance with publisher policies. Please cite only the published version using the reference above. Full terms of use are available: <http://www.bristol.ac.uk/red/research-policy/pure/user-guides/ebr-terms/>

# Numerical Investigation on Aerodynamic Noise of Flow past a Cylinder with Different Spanwise Lengths

Guanjiang Chen,<sup>1</sup> Bin Zang,<sup>1</sup> and Mahdi Azarpeyvand<sup>1</sup>

*Faculty of Engineering, University of Bristol, Bristol, BS8 1TR, United Kingdom*

(\*Electronic mail: nick.zang@bristol.ac.uk)

(Dated: 16 February 2023)

A numerical investigation is conducted on aerodynamic noise of flow past a circular cylinder with different spanwise lengths ( $0.5\pi D$ ,  $\pi D$ ,  $2\pi D$ ,  $4\pi D$ ) at  $Re = 10,000$ , where  $D$  is the diameter of the cylinder. The near-field pressure and velocity fields are predicted through Large Eddy Simulation (LES), then the acoustic analogy is used to obtain the far-field noise. The results show good agreements for both the near- and far-field with the data from in-house experiments and the literature. Though the spanwise length has limited influence on the power spectral density of the near-field velocity and pressure fluctuations at different spanwise locations, substantial differences are observed for the spanwise pressure coherence and near-wake structures. The  $0.5\pi D$  case shows primarily two-dimensional flow features immediately behind the cylinder compared to the other three cases, resulting in the overprediction of the spanwise pressure coherence, which has strong implications for the far-field noise prediction. With the spanwise length correction, the differences in overall noise magnitudes of the different cases diminish. Nevertheless, the  $2\pi D$  and  $4\pi D$  cases better capture the first and second harmonics of the vortex shedding and its associated directivities than the other two cases, showing the importance of sufficient spanwise lengths in predicting noise from flow past a cylinder.

## I. Introduction

Flow past a cylinder is one of the most studied aerodynamic problems in a wide range of engineering application, such as train pantographs, automotive axles, aircraft landing gears, *etc.* Its flow field consists of complex physical features: the transition of the boundary layer, the flow separation, the vortex shedding, the turbulent wake. The noise performance and the its mitigation strategies of the flow past a cylinder have also attracted increasing research and industrial interests with a significant need for high-fidelity methods to simulate the flow around the cylinder and predict the far-field noise. In the following, some previous studies are reviewed in terms of both the aerodynamic and aeroacoustic characteristics, though it should be noted that there are a large number of literature available on different aspects of the flow past a cylinder.

Many studies have been conducted to investigate the aerodynamic characteristics of the flow past a cylinder. The flow pattern is closely related to the Reynolds number,  $Re = U_\infty D / \nu$  based on the cylinder diameter  $D$ , the undisturbed freestream velocity  $U_\infty$ , and the kinematic viscosity  $\nu$ . Depending on the Reynolds number, the flow past a cylinder could be divided into the subcritical regime ( $400 < Re < 10^5$ ), the critical regime ( $10^5 < Re < 3 \times 10^5$ ), the supercritical regime ( $3 \times 10^5 < Re < 3 \times 10^6$ ), the transcritical regime ( $Re > 3 \times 10^6$ ). The studied Reynolds number in this paper is in the subcritical regime, where the turbulence transition happens in the separated shear layers<sup>1,2</sup>.

The Reynolds-averaged Navier–Stokes (RANS) simulation has been widely used in both research and industry due to its relatively low computational cost and fast solution time. More recently, highly resolved numerical methods, such as Large Eddy Simulation (LES), have become more readily available to researchers, which can achieve better resolution and accuracy for turbulent flows. In terms of the numerical scheme,

a number of LES studies have been conducted for the flow past a cylinder. Kim<sup>3</sup> carried out LES of the flow past a cylinder for Reynolds number from 3,000 to 140,000. It is concluded that the upwind-biased schemes introduced too much numerical dissipation. Non-dissipative central differencing was ideal for the LES of flow past a cylinder, however, it was known to be susceptible to producing unphysical oscillations in the solution fields. Therefore, a bounded central differencing (BCD) scheme was chosen to ameliorate the drawback of the central differencing scheme. Breuer<sup>4,5</sup> tried different numerical schemes in LES cases at  $Re = 3,900$ , which played an important role for the accuracy of the LES solutions. Central schemes of second- or fourth-order accuracy turned out to be well suited in LES, and upwind schemes was not recommended for such simulations. Lysenko *et al.*<sup>6,7</sup> carried out LES of the flow past a cylinder at  $Re = 3,900$  and 20,000. The filtered central differencing scheme, the BCD scheme and the LUST scheme were used to suppress the spurious wave, but the spectral analysis showed these schemes were too dissipative to keep the high-fidelity of the LES.

Different computational methods have also been studied and compared. Young and Ooi compared LES and URANS methods in simulating the flow past a cylinder at  $Re = 3,900$ <sup>8</sup>. The results of LES captured the flow field more accurately compared to the unsteady RANS (URANS) results. The authors argued that the improvement in LES was mainly due to the high spanwise resolution. They also found the result of URANS was very sensitive to the time step size. Wornom *et al.*<sup>9</sup> used Variational Multi-Scale Large Eddy Simulations (VMS–LES) to study the flow past a cylinder at  $Re = 3,900, 10,000$  and 20,000, with the Wall-Adapting Local Eddy-viscosity (WALE) subgrid-scale model. In the VMS–LES approach, the model was only applied to the smallest resolved scale cells, which were distinguished by the VMS formulation. The results showed that the methodology could accurately predict the aerodynamic forces around the cylinder and captured the flow features for the different Reynolds num-

bers. Zhang *et al.*<sup>2,10,11</sup> conducted a series of wall-resolved LES of the flow past a cylinder, using high-quality boundary layer grids and the WALE subgrid-scale model. The results show good agreement with the other LES and experimental data, and the flow separation and reattachment are well captured. For the solution convergence, Franke *et al.*<sup>12</sup> conducted a compressible LES for the flow past a cylinder at  $Re = 3,900$  and showed that the number of simulated vortex shedding periods should be larger than 200. Lysenko *et al.*<sup>6</sup> concluded 150 vortex shedding periods are necessary to achieve full convergence.

The size of the computational domain and the mesh resolution also have effects on the numerical results. The result of Kim<sup>3</sup> showed that the near-wake predictions were sensitive to the spanwise length of the computational domain and the spanwise mesh resolution. Khan *et al.*<sup>13</sup> conducted a LES research on the flow past a cylinder at  $Re = 3,900$ . They investigated the effects of the spanwise grid and the near-field grid size on the recirculation length, the angle of flow separation, and wake characteristics. The mesh resolution in the spanwise direction and the near-field grid had more influence on the simulation results than the spanwise length. The LES from Breuer<sup>14</sup> showed that the grid refinement did not significantly improve the agreement between the simulation and the experiment results, with regard to the drag coefficient, the recirculation length and the Strouhal number, but the improvement might be overridden by the modeling and discretization errors. Prsic *et al.*<sup>15</sup> simulated the flow past a cylinder at  $Re = 13,100$ . The results showed that the spanwise length of 4D was sufficient to capture the three-dimensional flow effects, and high spanwise mesh resolution did not change the captured flow significantly.

To compute the far-field noise numerically, hybrid CFD/CAA approach has been widely adopted and validated. Nitzkorski and Mahesh<sup>16</sup> proposed a dynamic end cap methodology for the Ffowcs-Williams and Hawkings (FW-H) acoustic analogy method, which could predict the far-field acoustic pressure when coupled with CFD. This method showed good accuracy and its predictive ability was much better when it is coupled with LES than coupled with URANS. Cianferra *et al.*<sup>17</sup> compared three acoustic analogy methods between the original FW-H formulation with volume integral, the porous FW-H and the Curle formulations for predicting the far-field noise of flow past a square cylinder. They concluded that the Curle and porous FW-H methods could be applied to the problems with neglectable compressibility effects. Zhang *et al.*<sup>18</sup> conducted wall-modeled LES coupled with the FW-H method for a cylinder and a rod-airfoil cases. They compared the noise results from integrating over a permeable surface with those from the solid surface of the bluff body, and found that the two results are almost identical. Hence, they suggested that it is satisfactory to employ solid body as the FW-H control surface for capturing the cylinder noise at low speeds. Zhang *et al.*<sup>2,11</sup> coupled the LES with direct numerical simulation and FW-H method to predict the far-field noise of the flow past a cylinder in the critical regime. The cross-correlation between the near- and far-field pressure fluctuations showed that the vortex shedding was the dominant noise source, while the

region above the cylinder close to the end of the transition shear layer and the shear layer in the near wake contributed more to the broadband component of the far-field noise.

Similar to the aerodynamic prediction, the size of the computational domain is crucial to the accuracy of the noise prediction. Karthik *et al.*<sup>19</sup> coupled the LES and FW-H methods to simulate the flow past a cylinder with five different spanwise lengths from 3D to 35D at  $Re = 84,770$ . The Strouhal number associated with the fundamental vortex shedding increased with larger cylinder span until a spanwise length of 25D, above which it remained constant at 0.19. Orselli *et al.*<sup>20</sup> simulated the flow past a cylinder using a two-dimensional RANS case and a three-dimensional LES case with a spanwise length of 2.5D. The simulated flow field results were then used to calculate the far-field acoustic pressure using the FW-H method. The three-dimensional LES results could capture the spanwise variations of the vortical structures, contributing to more accurate evaluation of the spanwise correlation lengths, which was needed for the sound pressure level (SPL) correction based on Kato's approach<sup>21</sup>. The corrected SPL results matched well with the experimental results from Revell *et al.*<sup>22</sup>. Jacob *et al.*<sup>23</sup> used the LES/FWH methods to simulate the flow past circular and non-circular cylinders. They also applied Kato's correction method to the noise results of the finite-span cylinder and showed that it was effective for the non-circular cylinder cases. Liu *et al.*<sup>24</sup> simulated the far-field noise of the flow past a cylinder, using the Delayed Detached-Eddy Simulation (DDES) coupled with the Curle's analogy, to assess the effects of different computational spanwise lengths on the predicted far-field acoustic pressure. The studied Reynolds number ranged from 26,700 to 367,000. In the critical regime, a spanwise length of 3D was shown to be sufficient to make accurate noise predictions, but in the subcritical range, a longer spanwise length was needed. Moreover, for cylinders with spanwise-varying cross-sectional shapes, the spanwise length used in the numerical set-up could also be a critical factor for both the flow and noise prediction due to intense flow variations along the spanwise direction<sup>25-27</sup>.

Though there have been some numerical investigations on the flow past a cylinder, it is still worthwhile to investigate a suitable set for the hybrid CFD/CAA method, including the numerical scheme, the subgrid-scale model of LES, the coupled acoustic analogy methods as well as the correction methods for the accurate prediction of its far-field noise. Specifically, there is no consensus on the influence of the spanwise length on the accuracy of the hybrid CFD/CAA method. Additionally, the effects of different spanwise lengths on the development and variations of vortical structures along the cylinder span are not fully understood, which play a vital role in the accurate noise prediction and correction. This paper aims to address the problem further by performing a series of LES of the flow past a cylinder with increasing spanwise lengths from  $0.5\pi D$  to  $4\pi D$  and predict the far-field noise using the FW-H acoustic analogy method. The spectral analysis is carried out on the near- and far-field results, and the relationship between the different spectral results is analyzed. Finally, the effects of different spanwise lengths on the near-

and far-field results are discussed. The layout of this paper is as follows: the computational setup are shown in Sec. II. The results are presented and discussed in Sec. III. Finally, Sec. IV summaries the effects of the spanwise lengths on the simulated aerodynamic and aeroacoustic results.

## II. Numerical methodology

In this section, the numerical set-up for the present study, including details of the solver schemes, mesh topology as well as the computational domain and boundary conditions will first be introduced. Reynolds-averaged Navier–Stokes (RANS) and Large Eddy Simulation (LES) were performed for the flow past a cylinder at  $Re = 10,000$  based on the cylinder diameter  $D$  and the freestream velocity  $U_\infty$ . To study the effects of spanwise length, four different spanwise lengths of the computational domain are applied, namely  $L_z = 0.5\pi D, \pi D, 2\pi D$  and  $4\pi D$ . The simulations were performed in OpenFOAM 6. The results of the Reynolds-averaged Navier–Stokes (RANS) simulations were used as initial input for the LES case. The aeroacoustic calculation is carried out using a dynamic library libAcoustics developed by Epikhin *et al.*<sup>28</sup>. The detail of the computation method, the computational domain, boundary conditions, mesh parameters and the libacoustics are presented as following.

### A. Numerical solver and schemes

In RANS cases, all turbulence scales are averaged, modeled by turbulence models. The LES uses a filtering procedure for the Navier–Stokes equations. The smallest scales of the exact solution are parametrized via a sub-grid-scale (SGS) model, and the larger-scale flow structures will be solved in the simulation. In addition to the sub-grid scale model, the mesh also plays a role as a filter that no flow with a scale smaller than the mesh size can be captured. According to the research of Rosetti *et al.*<sup>29</sup>, the  $k - \omega$  SST turbulence model is chosen for the RANS case. From studies of<sup>2,9,11</sup>, the WALE model showed a good ability to capture the near-wall flow around the cylinder, and the acoustic analogy results using LES results with WALE model as the input also showed a satisfactory accuracy. As a result, the WALE model is chosen for the LES study.

A second-order central-difference scheme, '*Gauss linear*', is used for the pressure and velocity gradient discretization in the RANS study. For the divergence schemes, the advection terms are discretized using a *Gauss limitedlinear* scheme, which is a central-difference scheme that limits towards upwind in regions of rapidly changing gradient. However, for the LES study, the *Gauss linear* scheme is used for both the divergence and gradient terms. All RANS simulations were performed using the steady-state simpleFoam solver while the pimpleFoam was chosen for LES, with a second-order implicit Euler method (*backward* scheme) for the time derivative. For both cases, the generalised geometric-algebraic

multi-grid (GAMG) solver is set as the numerical solver for the pressure, and the smoothSolver is used for other parameters including the velocity, the turbulence kinetic energy ( $k$ ), and the specific rate of turbulence dissipation ( $\omega$ ). More information on the numerical set-up could be found in<sup>30</sup>.

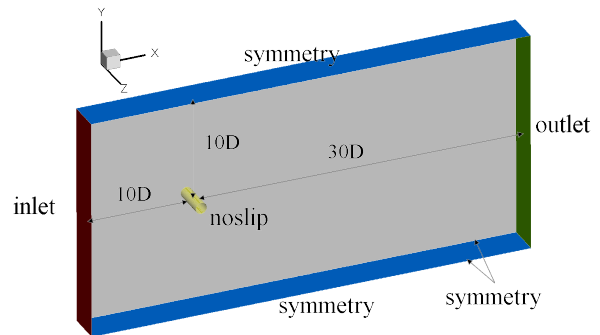


FIG. 1. The computational domain and boundary conditions.

### B. Computational domain, mesh and boundary conditions

The computational domain is shown in Fig. 1. The cylinder has a diameter  $D$  of 0.02 m. The Reynolds number based on the cylinder diameter ( $D$ ) is  $Re = 10,000$ , which is in the sub-critical range. The Reynolds number of the present study was chosen such that it is within the subcritical Reynolds number range. In this flow regime, some important characteristics are relatively independent of the Reynolds numbers, including drag coefficients, root-mean-square of lift coefficients and Strouhal numbers, as shown in<sup>3,24,31,32</sup>. Furthermore, an in-house experiment was performed at a similar Reynolds number to provide a direct comparison and validation of the acoustic results. Details of the experiments will be briefly discussed in Section II D.

The domain extends  $40D$  in the  $x$ -direction, while the inlet is located at the position  $10D$  upstream of the cylinder, and the outlet is  $30D$  downstream of the cylinder. In the  $y$ -direction, the width is  $20D$  with an equal distance of  $10D$  from the cylinder center to the top and bottom boundaries. In the spanwise  $z$ -direction, the four lengths from  $0.5\pi D$  to  $4\pi D$  are chosen. The size of the computational domain in this paper is comparable with the previous numerical investigations for the flow past a cylinder, as shown in Table. I. The top, bottom and side boundaries are set to symmetry conditions. For the velocity boundary conditions, a uniform freestream velocity of  $U_\infty = 7.6$  m/s is applied at the inlet and the no-slip wall is defined at the cylinder surface. A zero velocity gradient is set at the outlet, which will be switched to a fixed zero velocity for any potential reverse flow to ensure that the flow could only exit the computational domain at the outlet. For the pressure boundary conditions, the zero pressure gradient is set at the inlet and the cylinder surface. Coupled with the velocity boundary condition at the outlet, a zero pressure boundary condition is imposed by default with a zero pressure gradient

condition for any potential reverse flow. It is noted that the effects of wave reflections at boundaries are negligible due to the small flow Mach number and sufficiently large computational domain.

An overview of domain size and mesh details of the previous studies is summarised in Table I. The lengths of the computational domain in the  $x$ ,  $y$ ,  $z$  directions are  $L_x$ ,  $L_y$ ,  $L_z$  and  $\Delta z$  is the spanwise length of a mesh cell. Most previous studies used rectangular and circular domains. The rectangular domain consists of an O-type/rectangular hybrid mesh as shown in Fig. 2, while the O-type mesh is used around the cylinder. The total mesh size with the spanwise lengths from  $0.5\pi D$  to  $4\pi D$  are approximately from 8.5 million cells to 69.1 million cells.

The spanwise length  $\Delta z$  of a mesh cell is  $0.02D$ , which is comparable to the cell size used by other studies in Table I. The mesh near the cylinder surface is refined to make sure the  $y^+$  of the first layer cell near the cylinder surface is smaller than 1. The wall distance unit,  $y^+$ , is calculated as:

$$y^+ = \frac{u^* \times \Delta y}{\nu}, \quad (1)$$

where  $\nu$  is the kinematic viscosity of the fluid,  $u^*$  denotes the friction velocity based on the near wall velocity  $u_w$ ,  $u^* = \sqrt{u_w \times \nu / \Delta y}$ ,  $\Delta y$  is the normal distance from the surface to the cell center. Similarly, to compute  $z^+$  and  $x^+$ ,  $\Delta y$  is replaced with  $\Delta z$  and  $\Delta x$  along  $z$  and  $x$  directions, respectively, in Eq. 1. The  $y^+$  is smaller than 0.2;  $z^+$  is smaller than 6;  $x^+$  is smaller than 3.5, which meets the requirement for the wall-resolving LES<sup>35</sup>. Prior to the actual simulation, a mesh convergence test was conducted on the  $L_z = 0.5\pi D$  case with mesh sizes ranging from 3.8 million to 8.5 million. The results from pressure and velocity fields indicate that the present mesh is appropriate for the LES studies. The mesh convergence test results are not shown here for the sake of brevity.

The timestep for the calculation is  $5 \times 10^{-6}$ s, to make sure the Courant number is smaller than 1. The total simulation time,  $T$ , is 1.6 s, which is about 605 flow through cylinder period, defined as  $U_\infty T D$ . This is deemed sufficient for the initial disturbances to be dampened and the vortex shedding settles to the periodic nature<sup>6,8,12</sup>. The results of the final 0.6 s simulation are collected and used in the post-processing.

### C. Far-field noise computation and computational cost

Aeroacoustic analogy is a prevailing computational aeroacoustic (CAA) method to predict aerodynamic noise. Lighthill<sup>36,37</sup> first rearranged the Navier-Stokes equations to relate the free aerodynamic flow and the acoustics, which was the fundamental of the acoustic analogy. Curle<sup>38</sup> further considered the influence of solid boundary on the sound field. Ffowc Williams and Hawkings<sup>39</sup> deduced the equation considering the presence of arbitrarily moving surfaces, which is the Ffowc Williams-Hawkings (FW-H) equation. Farassat<sup>40</sup> derived the solutions of the FW-H equation with the surface sources moving at a subsonic speed, which are widely known as the Formulations 1 and 1A.

A dynamic library *libAcoustics* developed by Epikhin *et al.*<sup>28</sup> is used to calculate the far-field acoustic pressure from the LES results. The *libAcoustics* could be compiled independently of any modules in the OpenFOAM and it runs in real-time together with solvers. The time-series solution is used to calculate the far-field pressure fluctuations at certain points using the specified formula. To compare directly with the wind tunnel experiments, where the source and observers are stationary in the flow, a formulation based on the Garrick Triangle, referred as GT formulation, is more suitable<sup>41</sup>, and hence chosen in this study. The cylinder surface is used as the control (integral) surface in the acoustic analogy. The observer points are set on a circle of  $100D$  ( $r = 2$  m) from the center of the cylinder on the mid-plane ( $z/D = 0$ ).

All the simulations were conducted on the BlueCrystal High-Performance Computing Cluster at University of Bristol. The cluster is equipped with 525 Lenovo NX360-M5 computing node, each with two 14-core 2.4 GHz Intel E5-2680 CPUs and 128 GB of RAM, hence is capable of up to 600 trillion calculations per second. Due to the large mesh size of the LES cases, the simulations were performed in parallel on 112 to 336 processors for the case with  $L_z = 0.5\pi D$  to  $L_z = 4\pi D$ , respectively. The details of the computational resources needed for simulations performed in this study are summarized in Table II.

### D. Validation of aerodynamic performances

To help validate the numerical results, experiments on the flow past a cylinder were performed in-house in the aeroacoustic wind tunnel facility at University of Bristol<sup>42-44</sup>. The cylinder was mounted between two side plates, which were secured to the nozzle exit. A range of freestream velocities were tested from  $U_\infty = 7.6$  m/s to  $\approx 30$  m/s, resulting in a similar flow regime to the simulation. The inflow was considered laminar with a turbulence intensity of less than 0.2%. The far-field acoustics were collected via an overhead microphone arc. More details of the performance of the wind tunnel as well as the experimental set-up can be found in<sup>45,46</sup>.

To first validate the aerodynamic performance of the simulation results, the pressure coefficient  $C_p$  is compared with the available experimental data. The pressure coefficient of  $C_p$  is obtained from

$$C_p = \frac{p - p_\infty}{\frac{1}{2} \rho_\infty U_\infty^2}, \quad (2)$$

where  $p_\infty$  and  $p$  are the static pressure in the freestream and at the point where the pressure coefficient is evaluated, respectively,  $\rho_\infty$  is the freestream fluid density and  $U_\infty$  is the freestream fluid velocity.

Figure 3 shows the mean and the root-mean-square (rms) pressure coefficient from  $\theta = 0^\circ$  to  $\theta = 180^\circ$ , where  $\theta = 0^\circ$  denotes the windward and  $\theta = 180^\circ$  denotes the leeward of the cylinder. The experimental pressure coefficients in the literatures<sup>31,32</sup> and from the in-house experiments are provided for comparison. The value of  $C_p$  decreases from 1 at

TABLE I. Summary of computational domains and meshes used in previous studies.

	$L_x \times L_y$	$L_z$	$\Delta z$	Mesh type	$Re$
Kim <sup>3</sup>	$39D \times 21D$	$\pi D, 2\pi D$	$0.065-0.098D$	hybrid	3,000–14,000
Breuer <sup>4,14</sup>	$30D$	$\pi D$	$0.031-0.098D$	O-type	3,900
Lysenko <sup>6</sup>	$50D$	$\pi D$	$0.05D$	O-type	3,900
Franke <sup>12</sup>	$30D \times 20D$	$\pi D$	$0.095D$	hybrid	3,900
Young <sup>8</sup>	$40D \times 30D$	$\pi D$	$0.065-0.785D$	hybrid	3,900
Wornom <sup>9</sup>	$35D \times 40D$	$\pi D$	$0.03D$	hybrid	3,900–20,000
Khan <sup>13</sup>	$40D \times 20D$	$4D, 8D, 16D$	$0.08D$	hybrid	3,900
Prsic <sup>15</sup>	$32D \times 16D$	$4D$	$0.02-0.04D$	hybrid	3,900, 13,100
Jacob <sup>23</sup>	$29D \times 17D$	$3D$	$0.036D$	hybrid	19,800
Liu <sup>24</sup>	$31D \times 21D$	$3D$	$0.02-0.037D$	hybrid	26,700–150,000
Mani <sup>33</sup>	$35D$	$\pi D$	$0.0065D$	O-type	3,900, 10,000
Sharma <sup>34</sup>	$30D \times 20D$	$3D$	-	hybrid	14,000

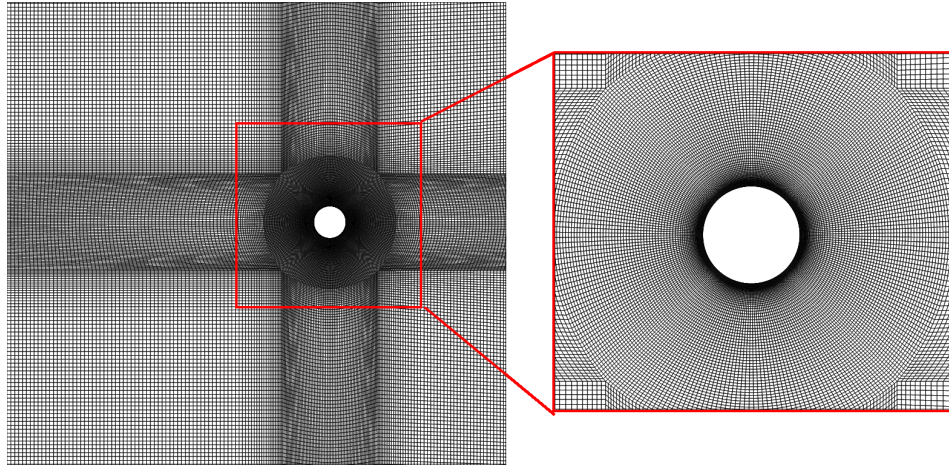


FIG. 2. The computational mesh on the x-y plane.

TABLE II. Summary of parallel running settings and computational costs.

Cases	Cells [million]	Nodes	Processors	Computational time [hours]
$L_z/D = 0.5\pi$	8.5	4	112	184
$L_z/D = \pi$	17.2	8	224	274
$L_z/D = 2\pi$	34.5	8	224	432
$L_z/D = 4\pi$	69.1	12	336	587

$\theta = 0^\circ$  to the lowest point at about  $\theta = 70^\circ$  under the favorable gradient. Then, the  $C_p$  value gradually increases with the adverse pressure gradient. This increasing trend stops at about  $\theta = 90^\circ$  as the flow separates from the cylinder surface. Subsequently, the  $C_p$  value shows a slightly decreasing trend, which is related to the small flow acceleration after the flow being separated. The  $C_p$  values of the cases with four different spanwise lengths are almost the same with each other. The simulated results such as the angle of the smallest  $C_p$  value and the flow separation point, where the slope of  $C_p$  changes from a positive value to zero, are in close agreement with the literature and the experimental data. The difference of the  $C_p$  value between the simulation results and the in-house experimental data collected in the aeroacoustic wind tunnel facility

at the University of Bristol is within 8%.

As shown in figure 3 (b), the  $C_{p,rms}$  of the cases with four different spanwise lengths show similar trends compared to the experimental data. The  $C_{p,rms}$  value is close to 0 at the stagnation point, then, the  $C_{p,rms}$  undergoes an increase until the angle close to the separation point. After the separation point, the  $C_{p,rms}$  decreases since the near wall pressure fluctuation weakens. There is a second peak of the  $C_{p,rms}$  value near  $\theta = 165^\circ$  which is considered to be related to the growth of the near wall pressure fluctuation caused by the vortex shedding process<sup>47</sup>. Though the LES generally over-predicts the  $C_{p,rms}$  value, the  $C_{p,rms}$  development trends of the LES cases are similar with the experimental data, i.e. having a primary peak around the separation point and a secondary one near the

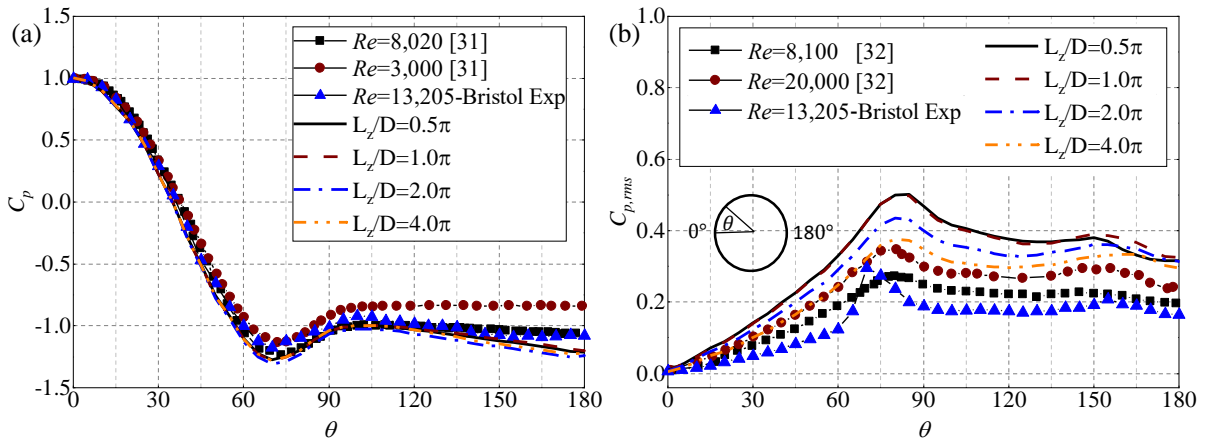


FIG. 3. (a) Mean and (b) rms pressure coefficients around the cylinder on the mid-plane  $z/D = 0$  at  $Re = 10,000$ .

wake. Considering the different measurement sets of experiments, the pressure values of LES cases with different spanwise lengths are considered to be reasonably accurate for subsequent analysis, though it is clear that the  $4\pi D$  case shows a noticeably closer  $C_{p,rms}$  to the experimental results.

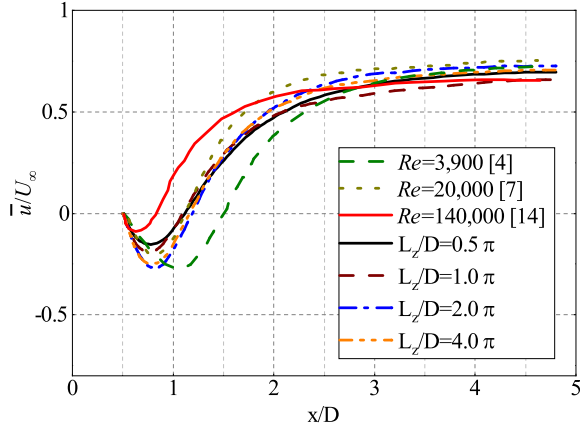


FIG. 4. Time-averaged streamwise velocity along the centerline ( $y/D=0$ ).

The time-averaged streamwise velocity along the centerline is presented in Fig. 4, and the results of three experimentally verified LES cases are provided for comparison<sup>4,7,14</sup>. The time-averaged velocity in the wake of the cylinder first decreases and then increases until recovering back to the freestream velocity. The results of LES cases with different spanwise lengths are within the result range between values at  $Re = 3,900$  and at  $Re = 140,000$  and close to the result of<sup>7</sup> at  $Re = 20,000$ . Since only a limited number of numerical studies have presented the wake velocity results along the centerline, results with similar Reynolds numbers to the present study were not available. Nevertheless, these comparisons establish that the centerline velocity results from the present simulation fall within the acceptable bounds found in the literature over the chosen Reynolds number range.

### III. Results and Discussions

The simulation results are shown in this section. Firstly, the near-field results are presented and compared with the experimental data either in-house or from the literature. Then, Proper Orthogonal Decomposition (POD) is applied to the near-field velocity of the cylinder to capture the dominant flow modes of the different spanwise length cases, which will contribute to a better understanding of the near-field flow structures and their implications to the noise prediction. Finally, the far-field results are presented and validated with experiments and the far-field noise directivity is analyzed.

#### A. Velocity and pressure fluctuations in the cylinder near-field

##### 1. Surface pressure power spectral density

The surface pressure power spectral density (PSD) at different circumferential angles around the cylinder surface on the mid-plane  $z/D=0$  and side planes are shown in Fig. 5, as a function of the Strouhal number. The side planes corresponding to the different spanwise length cases are from  $z/D=0.75$  to  $6.2$  for the  $L_z = 0.5\pi D$  to  $4\pi D$  cylinders, respectively. The surface pressure PSD is evaluated by the ‘*Pwelch*’ function in Matlab. The PSD data are also referenced to  $p_{ref} = 20\mu\text{Pa}$ . As shown in Fig. 5 (a), the cases with different spanwise lengths show very close surface pressure PSD results on the mid-plane  $z/D=0$ . From Fig. 5 (b), the surface pressure PSD on the side planes are consistent with that on the mid-plane. The broadband components and tonal components are comparable for the cases with different spanwise lengths, indicating that changing the spanwise length has limited influence on the vortex shedding frequency and strength in the present simulations.

The tonal peak at fundamental vortex shedding frequency ( $f_0$ ) and the first harmonic ( $f_1=2f_0$ ) are visible in the results. In the sub-critical Reynolds number range, the Strouhal num-

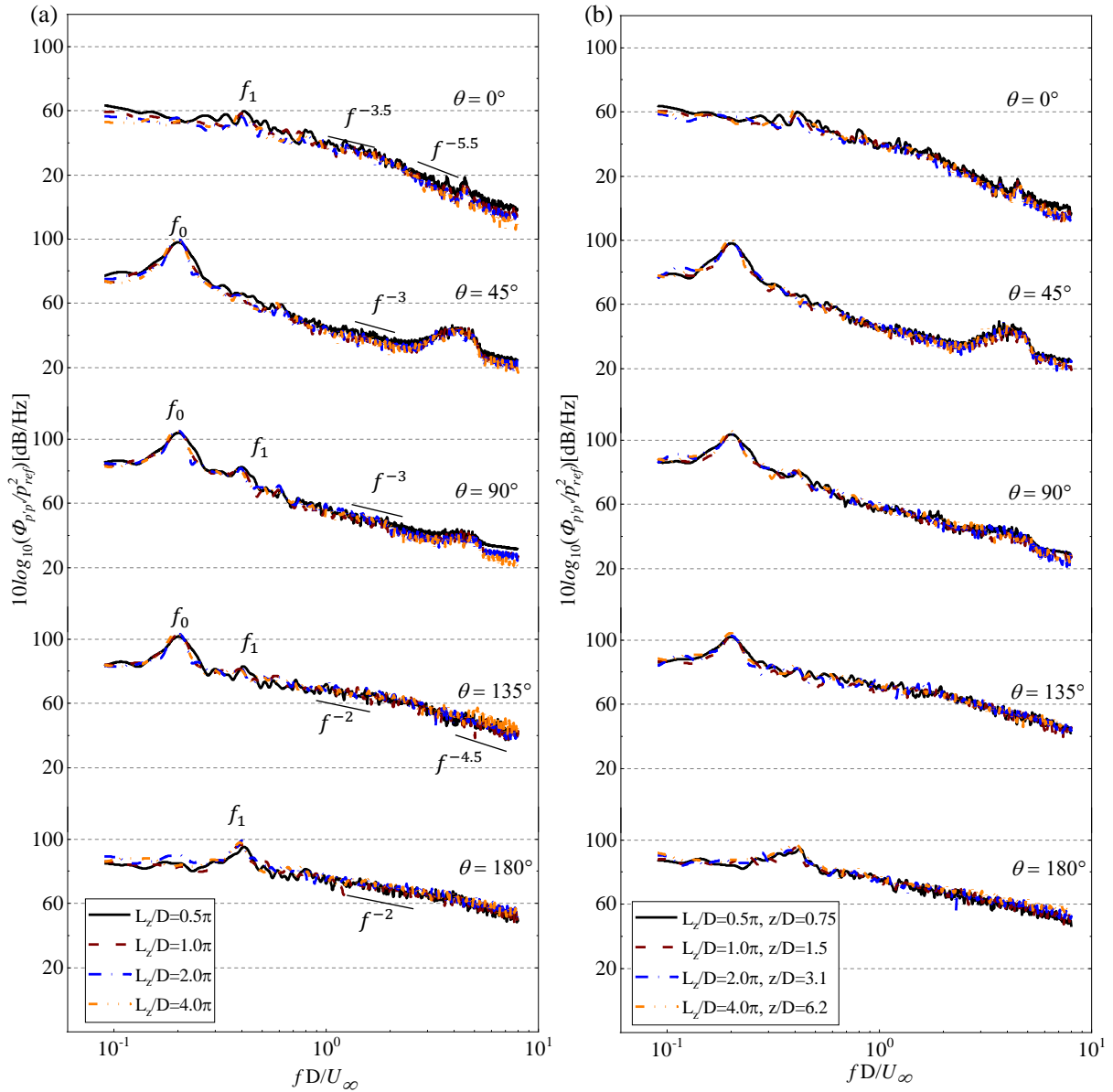


FIG. 5. Surface pressure power spectral density from the cases with different spanwise lengths on (a) the mid-plane  $z/D=0$  and (b) the side planes at different angles at  $Re=10,000$ .

ber ( $St = fD/U_\infty$ ) for the fundamental vortex shedding frequency is approximately 0.2. The tonal peak at the fundamental vortex shedding frequency ( $f_0$ ) protrudes about 20 dB above the broadband component of the surface pressure PSD at  $\theta = 45^\circ$ ,  $\theta = 90^\circ$  and  $\theta = 135^\circ$ . At these locations, the surface pressure fluctuation is mainly affected by the flow separation from the upper cylinder, associated with a full cycle of vortex shedding. As a result, the peak at the fundamental vortex shedding frequency ( $f_0$ ) is significantly higher than that of the first harmonic ( $f_1$ ). At  $\theta = 0^\circ$  and  $\theta = 180^\circ$ , the surface pressure fluctuation is affected equally by flow separation and vortex shedding from the upper and the lower half of the cylinder. Therefore, the frequency corresponding to the strongest surface pressure fluctuations at these two points is twice as

much as the fundamental frequency ( $f_0$ ), and the tonal peak at the first harmonic ( $f_1$ ) is obvious, associated with half a cycle of the vortex shedding.

Figure 6 shows the surface pressure PSD from the case with  $L_z = 4\pi D$  on the mid-plane ( $z/D=0$ ) at different angles at  $Re = 10,000$ . At  $\theta = 0^\circ$ , the broadband components and the tonal peak of the surface pressure PSD are obviously smaller than the results at other angles due to the considerably weak velocity and pressure fluctuations at the stagnation point. The broadband components increase dramatically from  $\theta = 0^\circ$  to  $\theta = 90^\circ$  as the near wall flow develops from the stagnation point to the separation point. Then, the broadband components grow further in magnitude in the post-separation region at  $\theta = 135^\circ$  and  $\theta = 180^\circ$  as the separated flow becomes more



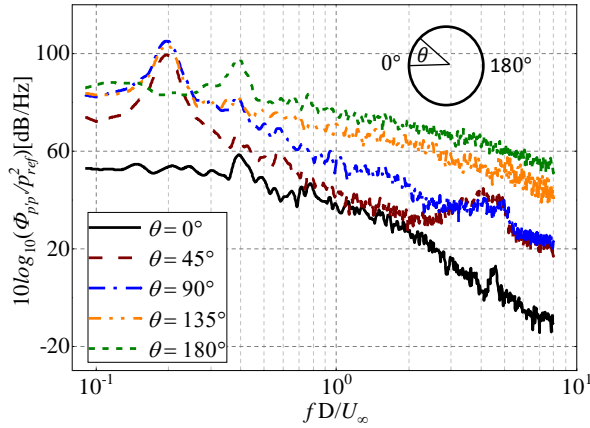


FIG. 6. Surface pressure power spectral density from the case with  $L_z = 4\pi D$  on the mid-plane  $z/D=0$  at different angles at  $Re = 10,000$ .

turbulent in this region, which intensifies the surface pressure fluctuations. The tonal peak reaches the highest point at  $\theta = 90^\circ$  and the frequency of the major tonal peak moves to the first harmonic at  $\theta = 180^\circ$ .

Overall, as expected, the broadband components decrease with increasing frequency. As shown in Fig. 5 (a) and Fig. 6, before the  $\theta = 90^\circ$ , the broadband components show a slope of  $f^{-3}$  in the middle frequency range around  $St = 1$  and  $f^{-5.5}$  around  $St = 6$ . At larger angles of  $\theta = 135^\circ$  and  $\theta = 180^\circ$ , the slope changes to  $f^{-2}$  in the middle frequency range and  $f^{-4.5}$  around  $St = 6$  since the broadband components associated with the turbulent fluctuations increase with increasing angle.

For the surface pressure PSD at  $\theta = 45^\circ$  in Fig. 5 and Fig. 6, a broadband hump is observed from  $St = 2.5$  to  $St = 4$ , which is considered to be the inception of the Kelvin–Helmholtz instability, according to Prasad and Williamson<sup>48</sup>. The Kelvin–Helmholtz instability has influences on the velocity and pressure fluctuations and the Kelvin–Helmholtz frequency follows a relationship with the fundamental vortex shedding frequency  $f_{KH}/f_0 = 0.0235 \times Re^{0.67}$ . In the present work, the Strouhal number for the  $f_{KH}$  is  $St_{KH} \approx 2.3$ , which is close to the frequency of the broadband hump of the pressure PSD at  $\theta = 45^\circ$ . As the broadband energy content of the surface pressure fluctuation increases with the angles, only a small hump is shown near  $St = 3$  at  $\theta = 90^\circ$  as seen in Fig. 6, and totally disappears at  $\theta = 135^\circ$  and  $\theta = 180^\circ$ , indicating that the signature of the Kelvin–Helmholtz instability is likely to be masked by the higher broadband energy contents. For the same reason, there is no noticeable broadband hump at  $St_{KH} \approx 2.3$  of the velocity PSD in the shear layer line, as will be shown later in Figs. 7 and 8.

## 2. Velocity fluctuation power spectral density

To assess the influence of different spanwise lengths on the velocity fluctuations, the power spectral density (PSD) of the

velocity in the x (streamwise) direction is presented in Fig. 7 at four locations downstream of the cylinder ( $x/D=0.5, 2, 5, 10$ ) along the centerline ( $y/D=0$ ) and the shear layer line ( $y/D=0.5$ ) on the side planes as defined in sec. III A 1. Only the results along side planes are presented because the PSD magnitudes in the side planes are consistent with that along the mid-plane for each case, and the velocity PSD on the mid-plane  $z/D=0$  of the case with  $L_z = 4\pi D$  is also plotted for comparison. Similar to the surface pressure PSD, the velocity PSD is evaluated by the ‘*Pwelch*’ function and referenced to freestream velocity of  $U_\infty = 7.6$  m/s. Overall, the cases with different spanwise lengths show comparable velocity PSD results along the mid-plane and side planes at the same x-y positions. The reason for such comparable velocity PSD is that the velocity fluctuations are related to the flow separation, the vortex shedding and the wake development, which are mainly two-dimensional features in the near wake of the cylinder.

Figure 8 shows the velocity PSD on the mid-plane ( $z/D=0$ ) from the case with  $L_z = 4\pi D$ . As shown in Fig. 8 (a), along the centerline ( $y/D=0$ ), there are no tonal components at the fundamental frequency  $f_0$ . The velocity along this line is equally affected by the vortex shedding both from the upper and the lower side of the cylinder, so the major fluctuation frequency is at the first harmonic  $f_1$ , twice as much as the fundamental frequency  $f_0$ . Moving downstream, the tonal peak value shows a decrease of 10 dB from  $x/D=0.5$  to  $x/D=10$  due to the weaker velocity fluctuation. As shown in Fig. 8 (b), the major tonal components of the flow velocity along the shear layer line ( $y/D=0.5$ ) are at the fundamental frequency  $f_0$ , which means the vortex shedding in the upper cylinder has obvious influence on the velocity fluctuation at these locations. The magnitude of the tonal peak decreases by 20dB from  $x/D=0.5$  to  $x/D=10$ , as the velocity fluctuations caused by the vortex shedding gradually weaken in the flow direction.

Moreover, clearly seen from Figs. 7 (a) and 8 (a), the velocity PSD decays with frequency at a slope of  $f^{-2}$  immediately after the first harmonic for all downstream locations. However, such decay at higher frequencies varies as the flow is convected downstream, since since the high-frequency velocity fluctuations dissipate quickly from near- to far-wake regions. At  $St$  greater than 3, the slope of velocity PSD spectra closest to the cylinder ( $x/D=0.5$ ) is  $f^{-2}$ , and changes from  $f^{-2}$  to  $f^{-5}$  in the near wake location of  $x/D=2$  and then further to  $f^{-8}$  in the furthest downstream location of  $x/D=5$ . From Fig. 8 (a), it can be seen that the slope at  $x/D=10$  is almost the same as that at  $x/D=5$ , which means the turbulence dissipation of high-frequency fluctuations of velocity becomes significantly weaker in the wake region beyond  $x/D=5$  and the decay rates are similar.

As for the broadband energy content along the shear layer line ( $y/D=0.5$ ) in Fig. 7 (b) and Fig. 8 (b), they are consistent with that of the centerline. The changing trends of the broadband components of the velocity PSD at  $y/D=0$  and  $y/D=0.5$  are comparable, which indicates the turbulence dissipation along the center and shear layer lines in the wake are similar. This is expected since both lines are in the region affected by the separated vortices.

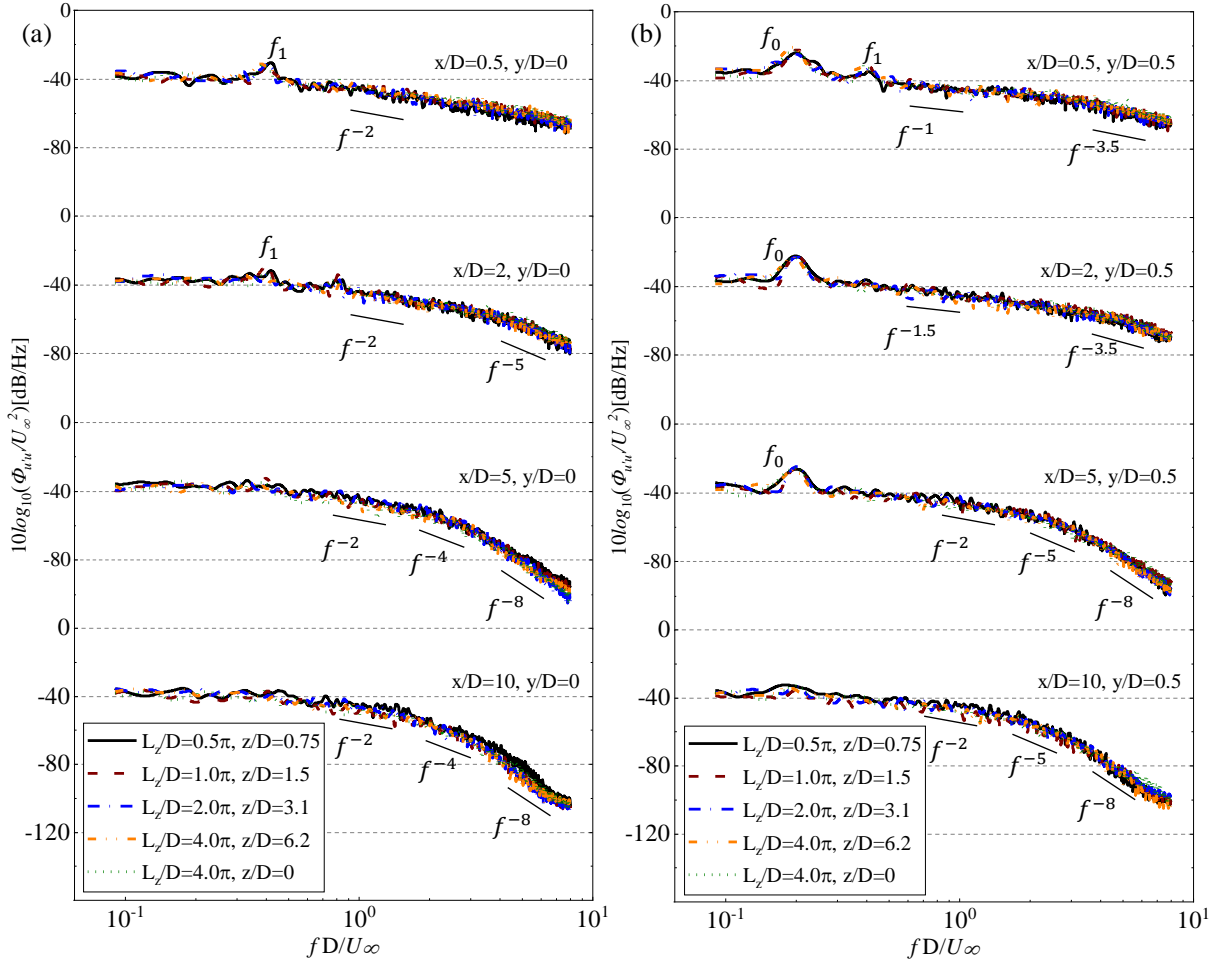


FIG. 7. Velocity power spectral density from the cases with different spanwise lengths on the side planes along (a) the centerline ( $y/D=0$ ) and (b) the shear layer line ( $y/D=0.5$ ) with different  $x/D$  from 0.5 to 10 at  $Re = 10,000$ .

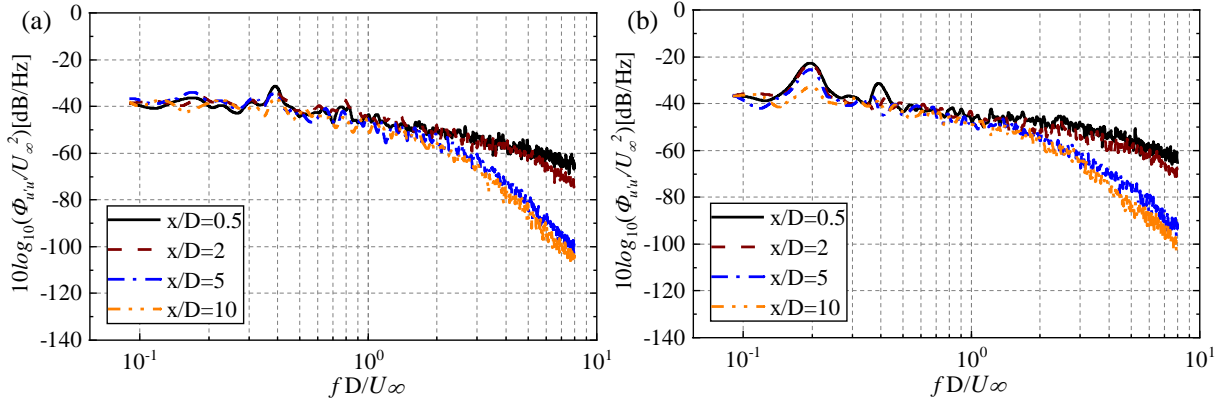


FIG. 8. Velocity power spectral density from the case with  $L_z = 4\pi D$  on the mid plane  $z/D=0$  along (a) the centerline ( $y/D=0$ ) and (b) the shear layer line ( $y/D=0.5$ ) with different  $x/D$  from 0.5 to 10 at  $Re = 10,000$ .

### 3. Spanwise variations of flow structures in the cylinder near-field

#### 3.1 Spanwise coherence of the surface pressure

When determining the effects of spanwise length on the

aerodynamic characteristics of the flow past a cylinder, the spanwise pressure coherence is useful in understanding the changes of flow development in the spanwise direction. Note that the pressure in this part refers to the surface pressure in

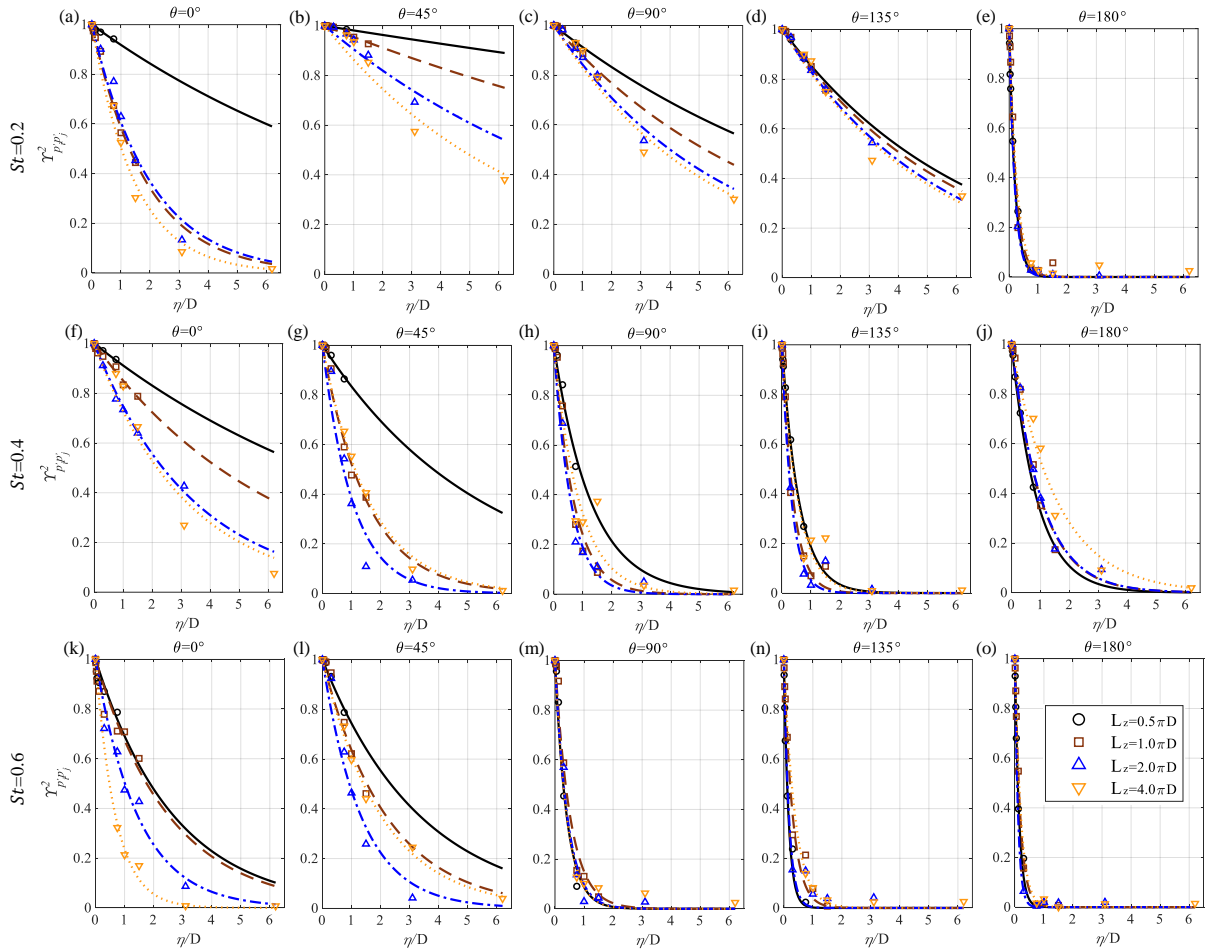


FIG. 9. Spanwise pressure coherence versus spanwise distances at [(a)-(e)] the fundamental vortex shedding frequency  $f_0$ , [(f)-(j)] the first harmonic  $f_1$ , and [(k)-(o)] the second harmonic  $f_2$ , at different angular positions from the cases with different spanwise lengths at  $Re = 10,000$ . Data are fitted with an exponential function ( $\exp(\alpha(\eta/D))$ ).

the near-wall region of the cylinder. The coherence is defined as

$$\gamma_{p_i p_j}^2 = \frac{|\Phi_{p_i p_j}(f)|^2}{\Phi_{p_i p_i}(f)\Phi_{p_j p_j}(f)}, \quad (3)$$

where  $p_i'$  and  $p_j'$  are pressure fluctuation signals at different spanwise locations.  $\Phi_{p_i p_i}$  and  $\Phi_{p_j p_j}$  are the power spectral density of  $p_i'$  and  $p_j'$ . Here,  $\Phi_{p_i p_j}$  is the cross power spectral density. A higher coherence value indicates two signals are more correlated.

Figure 9 shows the spanwise pressure coherence results in terms of the spanwise distances between two probes  $\eta/D$  at the fundamental vortex shedding frequency  $f_0$ , the first harmonic  $f_1$ , and the second harmonic  $f_2$ , at different angular positions of the cases with different spanwise lengths. The maximum spanwise distance is half of the spanwise length, i.e.  $\eta/D=0.75, 1.5, 3.1, 6.2$  for the cases with  $L_z = 0.5\pi D, 1\pi D, 2\pi D, 4\pi D$ . The results of the cases with  $L_z$  from

$0.5\pi D$  to  $2\pi D$  are exponentially fitted to  $\eta/D=6.2$ . In general, the coherence undergoes an increase from  $\theta = 0^\circ$  to  $\theta = 45^\circ$ , and then decreases from  $\theta = 45^\circ$  to  $\theta = 180^\circ$ . When  $\eta/D$  is 0.05, the coherence value is close to 1, indicating the two pressure signals are fully correlated. Then, the coherence decreases consistently with increasing spanwise distance, as expected. The coherence values of the  $0.5\pi D$  case are relatively high due to the short spanwise length, especially at  $\theta = 0^\circ$  to  $\theta = 45^\circ$ . The coherence values of the  $2\pi D$  and the  $4\pi D$  cases are smaller than the  $0.5\pi D$  and the  $\pi D$  cases due to the good ability to capture the three-dimensional variations of the vortex shedding in the wake, which will be clearly observed from the POD analyses.

The coherence decay rate can be described by the coherence length, which is determined when the coherence value drops to 0.5. A higher coherence length indicates a lower coherence decay rate. The coherence decay rates of the cases with four different spanwise lengths are comparable at  $\theta = 135^\circ$  and  $\theta = 180^\circ$ . At other angles, the coherence decays in similar trends for the  $\pi D$ ,  $2\pi D$  and  $4\pi D$  cases, and the coherence decay rate of the  $0.5\pi D$  case is relatively lower, especially at

$\theta = 0^\circ$  and  $\theta = 45^\circ$ . At  $\theta = 45^\circ, 90^\circ$  and  $135^\circ$ , the coherence decay rates at the fundamental frequency  $f_0$  are lower than that at the first and second harmonics ( $f_1$  and  $f_2$ ), while at  $\theta = 0^\circ$  and  $\theta = 180^\circ$ , the coherence decay rates of the first harmonic  $f_1$  are lower than that at the fundamental frequency  $f_0$  and the second harmonic  $f_2$ . The relatively lower coherence decay rate at each angle indicates more correlated pressure fluctuations, whose frequency is consistent with the major peaks of the surface pressure PSD, as shown in Figs. 5 and 6.

### 3.2 Q-criterion

The Q-criterion is commonly used to capture the coherent structures of the vortex shedding in the flow past a cylinder. Figure 10 shows the iso-surfaces of Q-criterion ( $Q=5 \times 10^6 \text{ s}^{-2}$ ) with contours of the velocity magnitude for the cylinder cases with different spanwise lengths. As can be seen, the laminar free-stream separates from the cylinder surface and sheds vortices in the wake. In the  $0.5\pi D$  and the  $\pi D$  cases, two-dimensional vortical structure with strong coherence along the spanwise direction can be clearly seen immediately downstream of the cylinder. These two-dimensional structures subsequently break up into three-dimensional vortices further downstream. On the other hand, for the  $2\pi D$  and the  $4\pi D$  cases, the flow structures exhibit strong three-dimensionality from the very beginning with smaller vortices forming after the flow separation, indicating their vortex shedding is much less coherent than those of the  $0.5\pi D$  and the  $\pi D$  cases. As will be seen later, the vortical structures observed from the Q-criterion are consistent with the three-dimensional POD modes. The  $2\pi D$  and the  $4\pi D$  cases show better ability to capture the three-dimensional flow features, which is important for the accurate prediction of the far-field noise.

### B. Three dimensional proper orthogonal decomposition of the near wake

Proper Orthogonal Decomposition has been widely employed to identify the energetic flow structures and various vortex shedding modes in flow past a cylinder. When applied to the three-dimensional velocity fields<sup>26,49-51</sup>, the POD modes are capable of discerning the dominant variations along the spanwise direction. However, there has not been any study comparing the three-dimensional POD modes of the flow past a cylinder with different spanwise lengths. In the present study, snapshot POD method<sup>52</sup> is used on the simulated instantaneous flow field with 6000 snapshots, capturing 227 flow through periods ( $U_\infty T$ )D. Sufficient probes are set around the cylinder near-wake to extract the velocity information: every  $0.05D$  in the  $z$  (spanwise) direction and a total of 9091 probes on the  $x$ - $y$  plane ( $-0.75 \leq x/D \leq 5, -2 \leq y/D \leq 2$ ). The mean velocity fields are considered as the zeroth mode of the POD. Subtracting the mean velocity, the fluctuating ve-

locities are arranged in a matrix  $U$  for the POD process:

$$U = |\mathbf{u}^1, \mathbf{u}^2, \dots, \mathbf{u}^N| = \begin{pmatrix} u_{11} & u_{12} & \cdots & u_{1N} \\ u_{21} & u_{22} & \cdots & u_{2N} \\ \vdots & \vdots & \ddots & \vdots \\ u_{M1} & u_{M2} & \cdots & u_{MN} \\ v_{11} & v_{12} & \cdots & v_{1N} \\ v_{21} & v_{22} & \cdots & v_{2N} \\ \vdots & \vdots & \ddots & \vdots \\ v_{M1} & v_{M2} & \cdots & v_{MN} \\ w_{11} & w_{12} & \cdots & w_{1N} \\ w_{21} & w_{22} & \cdots & w_{2N} \\ \vdots & \vdots & \ddots & \vdots \\ w_{M1} & w_{M2} & \cdots & w_{MN} \end{pmatrix}, \quad (4)$$

where  $u, v, w$  are the three fluctuating velocity components in the  $x, y, z$  direction. The snapshot number is  $N$  and the probe number is  $M$ .

The autocovariance matrix  $C$  is created as

$$C = U^T U, \quad (5)$$

and the corresponding eigenvalues  $\lambda$  and eigenvectors  $P$  of  $C$  could be solved by

$$C P_i = \lambda_i P_i. \quad (6)$$

The eigenvalues are sorted in descending order as

$$\lambda_1 > \lambda_2 > \lambda_3 > \dots > \lambda_N. \quad (7)$$

The energy of the POD mode is proportional to the corresponding eigenvalue, so the first mode represents the most energetic flow structure. The  $i^{\text{th}}$  order POD mode  $\psi_i$  is constructed by the velocity matrix  $U$  and the eigenvector  $P_i$  corresponding to eigenvalue  $\lambda_i$ ,

$$\psi_i = \frac{U P_i}{\|U P_i\|}. \quad (8)$$

The velocity field of a given snapshot could thus be reconstructed with the POD modes  $\psi_1, \psi_2, \dots, \psi_N$  and time coefficients  $k_i^n$  of  $\psi_i$ ,

$$\mathbf{u}^n = \sum_{i=1}^N \psi_i k_i^n = \Psi \mathbf{k}^n. \quad (9)$$

Note that  $n$  is the number of snapshots from 1 to  $N$ ,  $\Psi$  is  $[\psi_1, \psi_2, \dots, \psi_N]$ ,  $\mathbf{k}^n = [k_1^n, k_2^n, \dots, k_N^n]^T$ . The vector normalization is conducted on the mode  $\psi_i$ . Then,  $\Psi$  satisfies  $\Psi^T \Psi = I$ , and the time coefficients could be calculated from  $\mathbf{k}^n = \Psi^T \mathbf{u}^n$ .

The normalized eigenvalues of the first 10 POD modes are shown in Fig. 11, which could be considered as the percentage of the energy associated with the mode to the total fluctuating energy of the flow. The first few POD modes could be grouped in pairs such as modes 1-2 and modes 3-4 since they have comparable eigenvalues and similar flow structures.

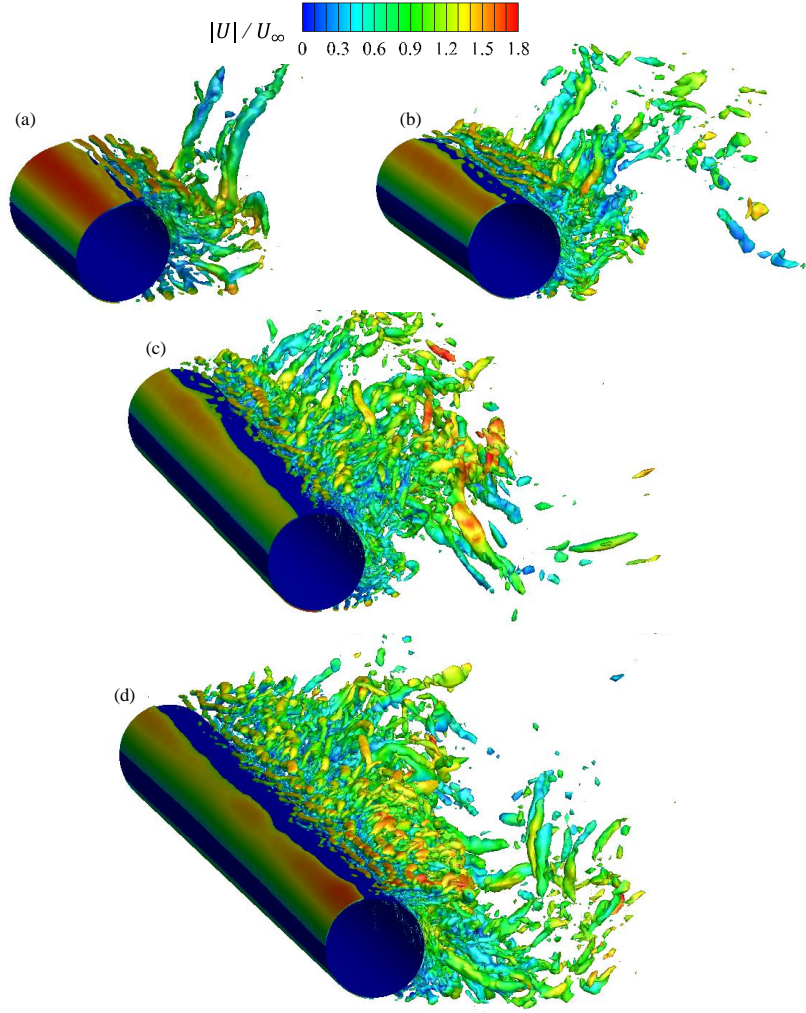


FIG. 10. Iso-surfaces of Q-criterion of  $Q=5 \times 10^6 \text{ s}^{-2}$  with contours of the velocity magnitude from the cases with spanwise lengths of (a)  $0.5\pi D$ , (b)  $\pi D$ , (c)  $2\pi D$  and (d)  $4\pi D$  at  $Re = 10,000$ .

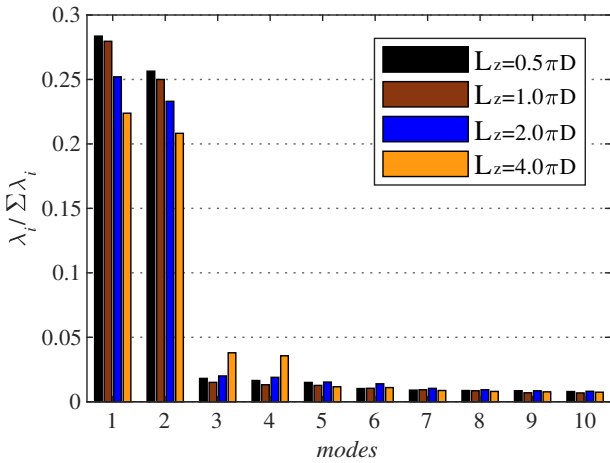


FIG. 11. The eigenvalue distribution of the first 10 POD modes from the cases with different spanwise lengths at  $Re = 10,000$

It can be concluded that the first mode pair contributes much more to the total energy than the other modes. In agreement with previous studies<sup>53–56</sup>, the first mode pair of the flow past a cylinder could be related to the fundamental vortex shedding, as shown in Figs. 13 and 14. Note that the vortex shedding in this section refers to the fundamental vortex shedding.

When the spanwise length increases, the energy percentage of the first two modes decreases, while that of mode 3 and mode 4 increases, especially for the  $4\pi D$  case. The case with longer spanwise lengths could capture more three-dimensional flow structures. Subsequently, more energy is distributed to higher modes, which represents the less coherent three-dimensional vortex shedding, as shown in the modes 3 and 4 of the case with spanwise lengths from  $\pi D$  to  $4\pi D$  in Fig. 15. In this section, the three-dimensional vortex shedding refers to the vortex shedding with obvious spanwise variations, while the two-dimensional vortex shedding refers to the vortex shedding with high coherence in the spanwise direction.

The spectra of time coefficients of the first 4 modes in

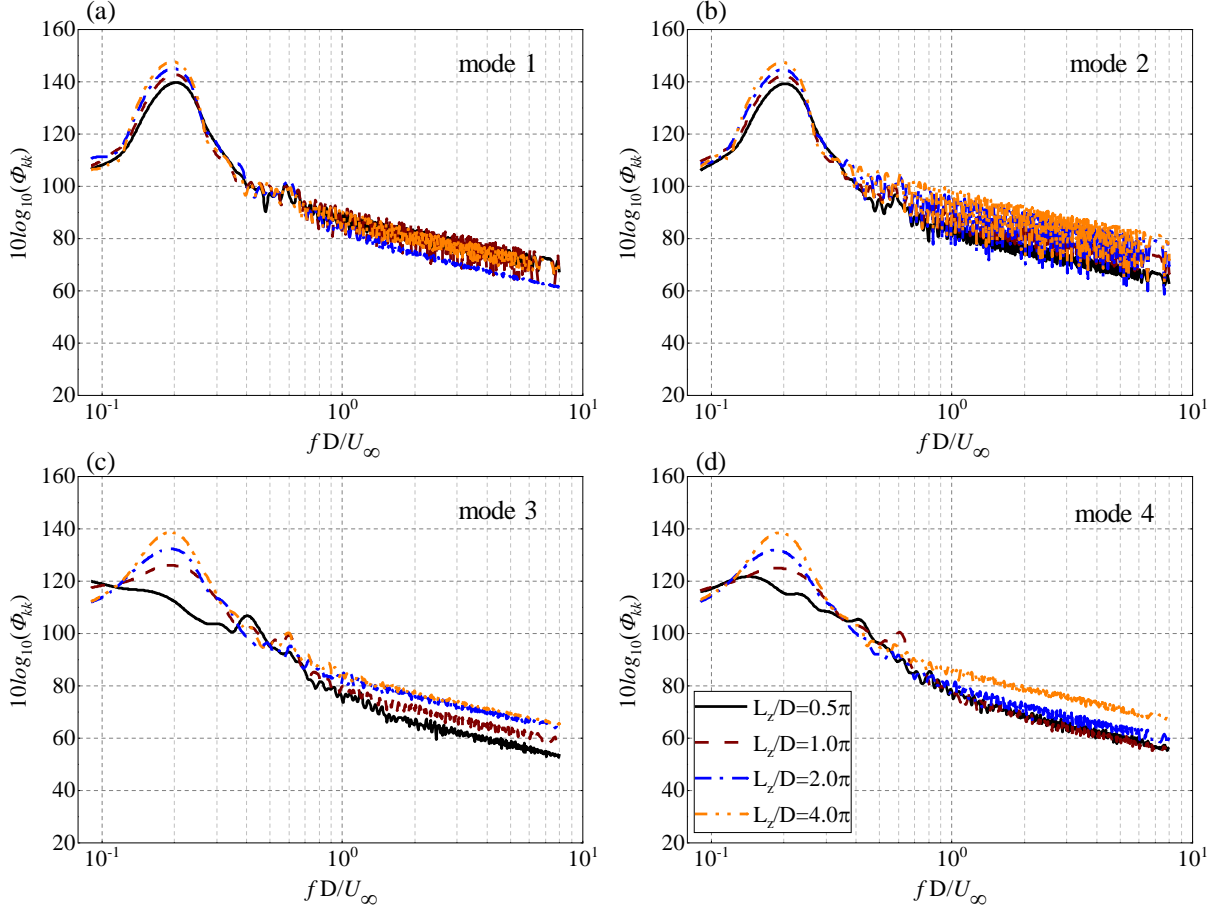


FIG. 12. Spectrum of time coefficients of (a) mode 1, (b) mode 2, (c) mode 3, (d) mode 4 from the cases with different spanwise lengths at  $Re = 10,000$ .

Fig. 12 reveal the energy-frequency information associated with the modes. The mode 1 and mode 2 have dominant peaks at the fundamental vortex shedding frequency of  $St = 0.2$ , which corresponds well with the flow structures of these two modes in Figs. 13 and 14, and it is the most energetic flow structure as shown in Fig. 11. For mode 3 and mode 4, the cases with spanwise lengths from  $\pi D$  to  $4\pi D$  still show peaks at  $St = 0.2$ , and this spectral peak is more obvious with longer spanwise lengths. The  $0.5\pi D$  case has a small peak at the first harmonic  $St = 0.4$  in the mode 3 rather than the fundamental vortex shedding frequency, while the mode 4 of the  $0.5\pi D$  case has no spectral peaks. This indicates that the  $0.5\pi D$  case mainly captured the two-dimensional vortex shedding that is predominantly captured in mode 1 and mode 2, and there is very minimal three-dimensional vortex shedding flow structures in mode 3 and mode 4.

Figure 13 shows the flow structure related to the first and second y-velocity mode with iso-surfaces at  $\psi=0.1$  (red) and  $\psi=-0.1$  (blue) for the cases with spanwise lengths from  $0.5\pi D$  to  $4\pi D$ . Note that for each velocity component, the maximum absolute mode value is normalized to 1, making it easier to compare those from other modes. The mode 1 and mode 2 consist of cylindrical flow structures, which are comparable to

modes in the previous studies<sup>26,49–51</sup>. The positive and negative regions appear alternating due to the periodicity of the vortex shedding, and the size of vortex increases along the streamwise direction. Overall, the mode 1 and mode 2 show strong coherent flow structures in the spanwise direction, as the iso-surface largely retains a cylindrical shape along the spanwise length. The  $0.5\pi D$  case shows the highest coherence and the mode near the cylinder is almost uniform along the spanwise direction, while in the  $\pi D$  case, some spanwise variations of flow structures near the cylinder could be seen. More spanwise variations of flow structures near the cylinder are found in the  $2\pi D$  case and the  $4\pi D$  case, meaning that these two cases capture more three-dimensional flow features in the near-wake vortex shedding.

The first and second velocity POD modes on the mid-plane  $z/D=0$  of the  $0.5\pi D$  case and the  $4\pi D$  case are shown in Fig. 14. The x and y-velocity modes are similar to the two-dimensional POD modes in literature<sup>49,54,57</sup>. Overall, the flow structures in mode 1 and mode 2 of the  $0.5\pi D$  case are comparable with that of the  $4\pi D$  case. Furthermore, the flow structures of mode 1 and mode 2 are in a pair, with a phase shift between the two modes.

For the y-velocity mode, the mode distribution is sym-

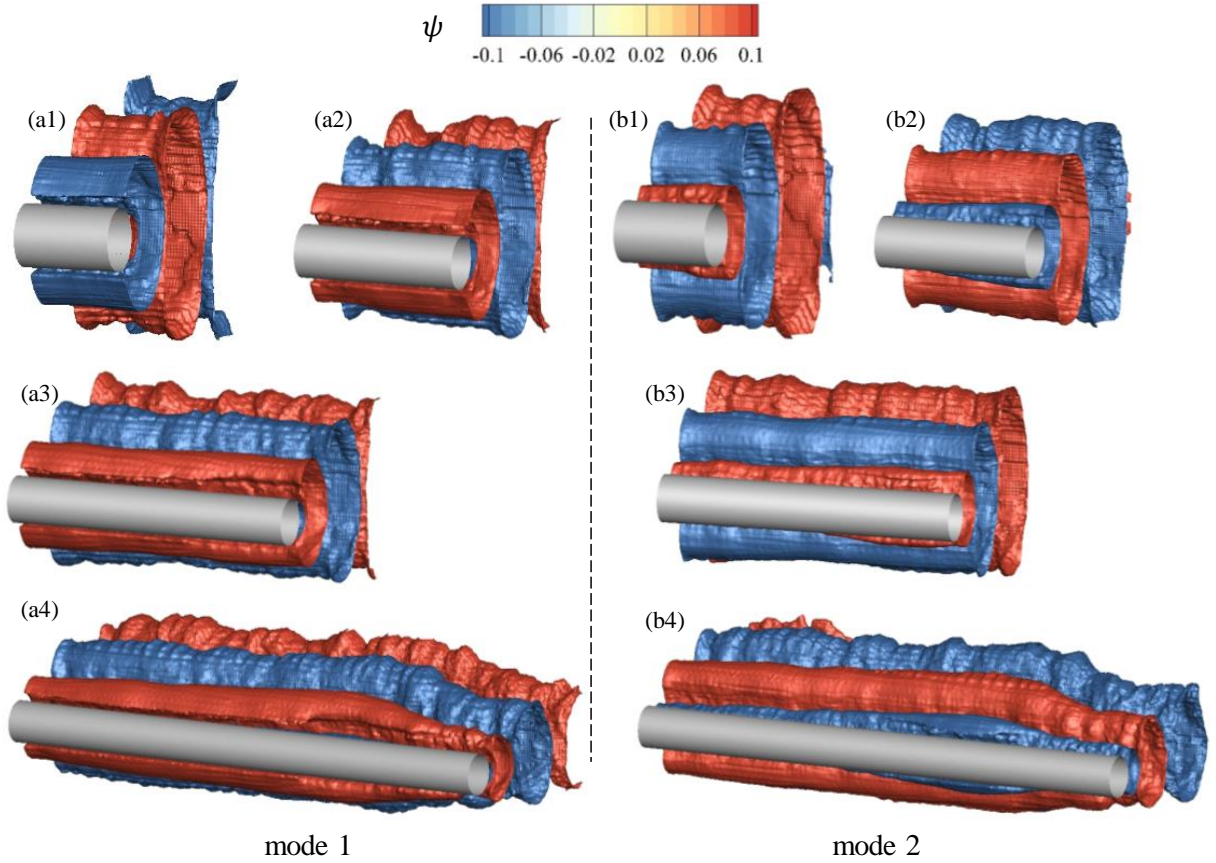


FIG. 13. Iso-surfaces of  $y$ -velocity component POD mode 1 (a1-a4) and mode 2 (b1-b4) at  $\psi=0.1$  (red) and  $\psi=-0.1$  (blue) from the cases with spanwise lengths of  $0.5\pi D$  (a1, b1),  $\pi D$  (a2, b2),  $2\pi D$  (a3, b3) and  $4\pi D$  (a4, b4) at  $Re = 10,000$ .

metry about the centerline  $y/D=0$ , consistent with the three-dimensional distribution in Fig. 13. For the  $x$ -velocity mode, the flow structures in mode 1 and mode 2 are anti-symmetrical about the centerline  $y/D=0$ . The shear layers could be seen near the upper and lower sides of the cylinder, and the round shape flow structures are related to the vortex shedding. The flow structure of the  $z$ -velocity mode is not as clear as its counterparts due to weaker velocity fluctuations in the spanwise direction. Nevertheless, it could be seen that the flow structures of the  $z$ -velocity mode are anti-symmetry about the centerline, and they expand along the flow direction.

Figure 15 shows the flow structure related to the third and fourth  $y$ -velocity mode with iso-surfaces at  $\psi=0.1$  (red) and  $\psi=-0.1$  (blue) for the cases with spanwise lengths from  $0.5\pi D$  to  $4\pi D$ . The flow structures of mode 3 and mode 4 are much less coherent than that of the first two modes. For the case with spanwise lengths of  $\pi D$ ,  $2\pi D$  and  $4\pi D$ , the major flow structures are in cylindrical shape related to the vortex shedding, especially for the  $2\pi D$  and  $4\pi D$  cases. But compared with the mode 1 and mode 2 in Fig. 13, obvious spanwise variations of flow structures are captured in the mode 3 and mode 4 with iso-surfaces disappearing at some locations, most discernible in the  $4\pi D$  case. It can be inferred that the three-dimensional vortex shedding structures are captured in the mode 3 and mode 4 rather than mode 1 and mode 2 because

these structures are less coherent and energetic than the two-dimensional ones. For the  $0.5\pi D$  case, the mode 3 and mode 4 flow patterns are not related to the vortex shedding since the vortex shedding is almost fully captured in the mode 1 and mode 2, as shown in Fig. 12. Nevertheless, the mode patterns of the  $0.5\pi D$  case still show high coherent flow structures near the cylinder in the mode 3, where the iso-surface keeps in the shape along the spanwise length.

The two-dimensional distribution of mode 3 and mode 4 of the  $0.5\pi D$  case and the  $4\pi D$  case are shown in Fig. 16. The modes of the  $0.5\pi D$  case are plotted on the mid-plane  $z/D=0$ , and the modes of the  $4\pi D$  case are plotted on the plane at  $z/D=3$ , where the vortex shedding is more obvious as shown in Fig. 15. The primary flow structures of mode 3 and mode 4 of the  $4\pi D$  case are similar to those of mode 1 and mode 2, associated with the vortex shedding. With the frequency characteristics in Fig. 12, it could be concluded that the flow structures of mode 1-4 of the  $4\pi D$  case are dominated by the fundamental vortex shedding with the frequency at  $St = 0.2$ . The first four modes of the  $\pi D$  and  $2\pi D$  cases show similar features with a dominant frequency of  $St = 0.2$ .

For the  $0.5\pi D$  case however, the mode patterns of  $y$ -velocity components are anti-symmetry about the centerline  $y/D=0$ , while that of the  $x$ -velocity components are symmetry about the centerline, which is contrary to that of the  $4\pi D$

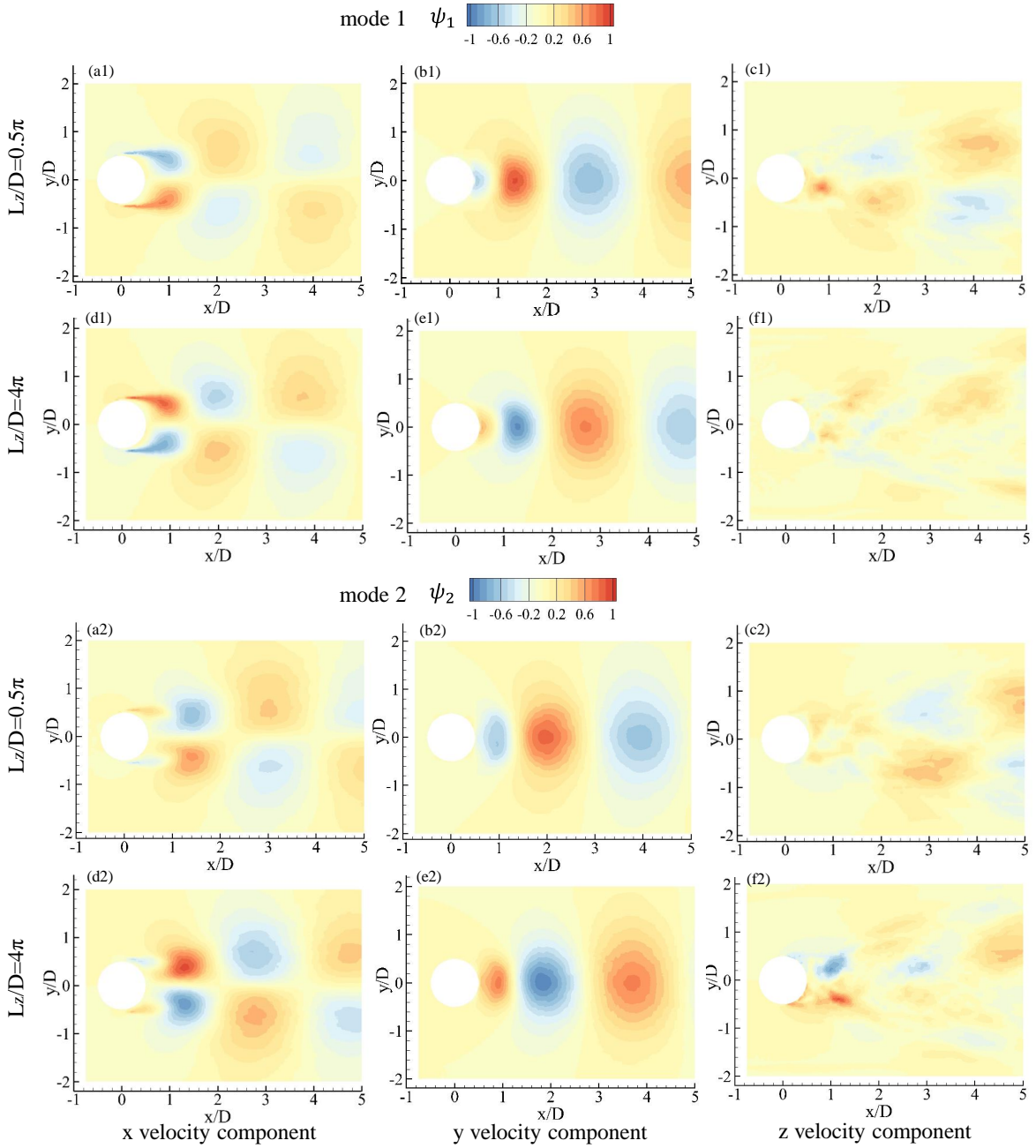


FIG. 14. POD modes 1 (a1-f1) and mode 2 (a2-f2) from velocity fields for the cases with spanwise lengths of  $0.5\pi D$  (a1-c1, a2-c2) and  $4\pi D$  (d1-f1, d2-f2) on the mid-plane of  $z/D=0$  at  $Re = 10,000$ .

case. This mode pattern occurs in the mode 3 of the study of Kourentis *et al.*<sup>57</sup>, which is considered to be related to the first harmonic, especially for the mode 3, consistent with the spectral peak at the first harmonic in Fig. 12(c). The  $z$ -velocity components of mode 3 and mode 4 show similar features to mode 1 and mode 2.

Due to the shorter spanwise length, the coherence of the  $0.5\pi D$  case is relatively higher than the other three cases as shown in Fig. 9. The flow structures of modes of the  $0.5\pi D$  case are also more coherent, and the spanwise variations of

the flow structures are much less than the other cases. As a result, the vortex shedding in the  $0.5\pi D$  case is mainly two-dimensional and just occurs in the first two modes. On the contrary, three-dimensional flow features are well captured in the other three cases, especially the  $2\pi D$  and  $4\pi D$  cases. A better simulation of the three-dimensional flow structures will benefit the more accurate noise prediction, which will be shown in the next section.



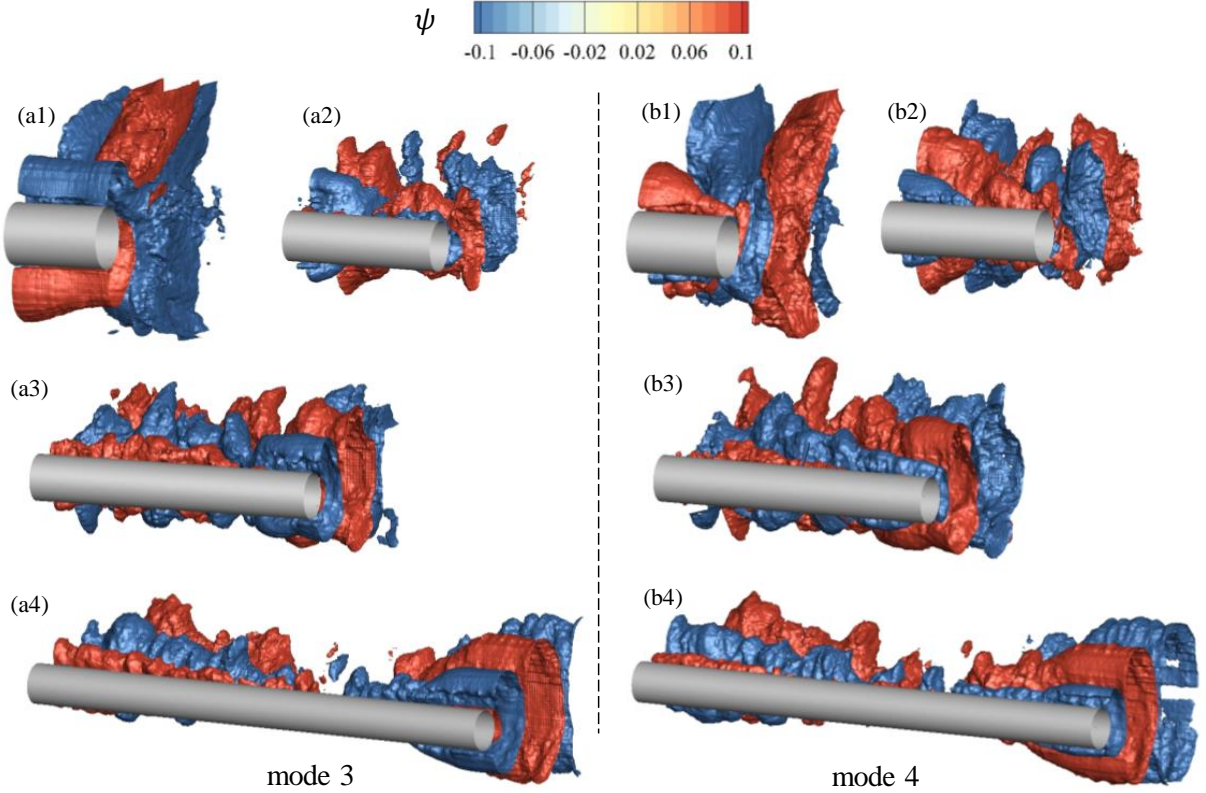


FIG. 15. Iso-surfaces of y-velocity component POD mode 3 (a1-a4) and mode 4 (b1-b4) at  $\psi=0.1$  (red) and  $\psi=-0.1$  (blue) from the cases with spanwise lengths of  $0.5\pi D$  (a1, b1),  $\pi D$  (a2, b2),  $2\pi D$  (a3, b3) and  $4\pi D$  (a4, b4) at  $Re = 10,000$ .

### C. Far-field acoustic prediction

With the far-field acoustic pressure from LES with *libAcoustics* module, the far-field acoustic pressure PSD is evaluated by the ‘*Pwelch*’ function in Matlab as  $10 \log_{10}(\Phi_{p'p'}/p_{ref}^2)$ , where  $p'$  is the far-field acoustic pressure fluctuations, and  $p_{ref} = 20 \mu\text{Pa}$ . The overall sound pressure level (OASPL) is calculated by  $\text{OASPL} = 10 \log_{10} \int (\Phi_{p'p'}/p_{ref}^2) df$ , where  $f$  is frequency. In this section, the PSD and OASPL of the far-field acoustic pressure are analyzed. The simulated results are corrected to compare with experimental results. Note that the acoustic pressure in this section refers to the far-field acoustic pressure.

#### 1. Spanwise length corrected acoustic power spectral density

The acoustic pressure is proportional to the integral of the force on the control surface. To compare the PSD magnitudes of the cases with different spanwise lengths, a spanwise length correction is needed. The correction method of Kato *et al.*<sup>21</sup> is used to estimate the additional noise generated by the longer part of the cylinder span, taking into account the spanwise coherence. Note that the method of Kato is designed for the sound pressure level ( $\text{SPL} = 10 \log_{10}(p'/p_{ref})^2$ ). As both PSD

and SPL are proportional to  $\log_{10}(p'^2)$ , the SPL correction as follows is also suitable with the PSD magnitude as:

$$\begin{cases} L_c < L_s, & \Delta\text{PSD} = 10 \log_{10}(L/L_s) \\ L_c \leq L_s < L, & \Delta\text{PSD} = 10 \log_{10}(L_c/L_s)^2 + 10 \log_{10}(L/L_c) \\ L \leq L_c, & \Delta\text{PSD} = 10 \log_{10}(L/L_s)^2. \end{cases} \quad (10)$$

where  $L_s$  is the length of the computational domain;  $L$  is the spanwise length which is taken into account in the correction ( $4\pi D$  for the spanwise length corrected PSD).  $L_c$  is the coherence length. The flow is considered to be highly correlated when the spanwise length is within  $L_c$ . It is assumed that the correlated flow in the same phase angle contributes more to the noise magnitude than the uncorrelated flow, so the part of  $L$  within  $L_c$  relates to  $(L/L_s)^2$ , while the part longer than  $L_c$  relates to  $(L/L_c)$ . The studies of Seo *et al.*<sup>58</sup> and Orselli *et al.*<sup>20</sup> showed that it was possible to replace the spanwise coherence length of the far-field acoustic pressure by the coherence length of the surface pressure. In the present study,  $L_c$  is determined when the spanwise pressure coherence drops to a critical value of 0.5 according to Fig. 9, the same as that used by Kato *et al.*<sup>21</sup>. Moreover, the coherence length of the surface pressure at  $\theta = 180^\circ$  is used for the correction of acoustic results at polar angles of  $\theta = 0^\circ$  and  $\theta = 180^\circ$ , while the coherence length of the surface pressure at  $\theta = 90^\circ$  is used for

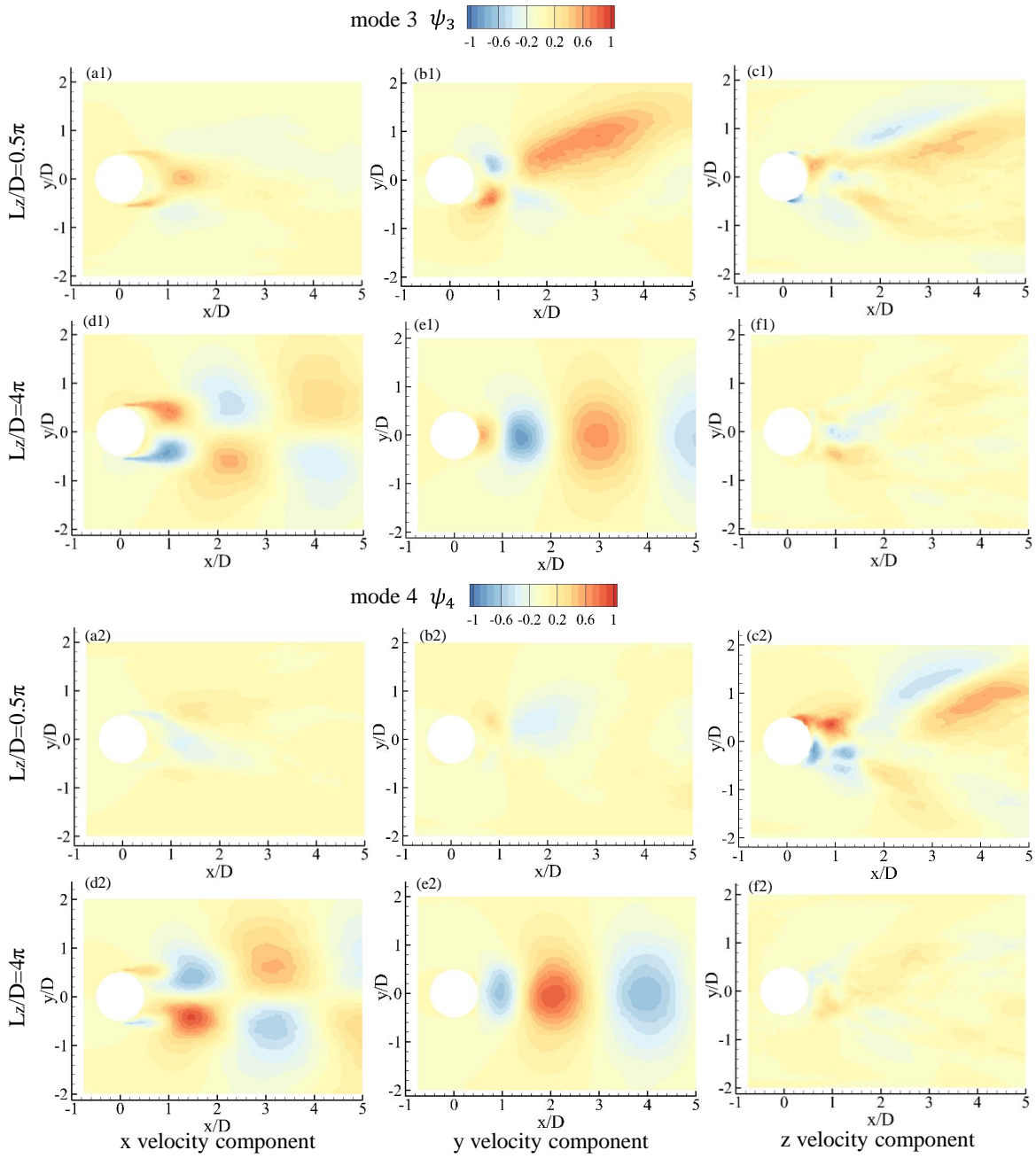


FIG. 16. POD modes 3 (a1-f1) and mode 4 (a2-f2) from velocity fields for the cases with spanwise lengths of  $0.5\pi D$  (a1-c1, a2-c2) and  $4\pi D$  (d1-f1, d2-f2) on the mid-plane of  $z/D=0$  at  $Re = 10,000$ .

all other angles. This is mainly due to the fact that at  $\theta = 0^\circ$  and  $\theta = 180^\circ$ , the acoustic pressure fluctuations are more influenced by the symmetric fluctuations along the  $x$ -direction (*i.e.*, drag).

The spanwise length corrected PSD is shown in Fig. 17. After the spanwise length correction, the PSD magnitudes in the broadband frequency range become close between the cases with different spanwise lengths. For the tonal peaks, the  $2\pi D$  case and the  $4\pi D$  case protrude more than their counterparts, and the discrepancy is within 3.17 dB/Hz at  $St = 0.2$

and 7.52 dB/Hz at  $St = 0.4$ . The frequency of the tonal peak is related to the lift and drag fluctuations. Note that the lift fluctuation is related to the fundamental vortex shedding frequency ( $f_0$ ) and the even-number harmonics ( $f_2 = 3f_0, \dots$ ), while the drag fluctuation is related to the odd-number harmonics ( $f_1 = 2f_0, f_3 = 4f_0, \dots$ ), which can be attributed to the fact that the vortices shed from either side of the cylinder give the same contribution to the drag and opposite contributions to the lift. Therefore, for polar angles located at one side of the cylinder from  $\theta = 45^\circ$  to  $135^\circ$ , the dominant peak is at fun-

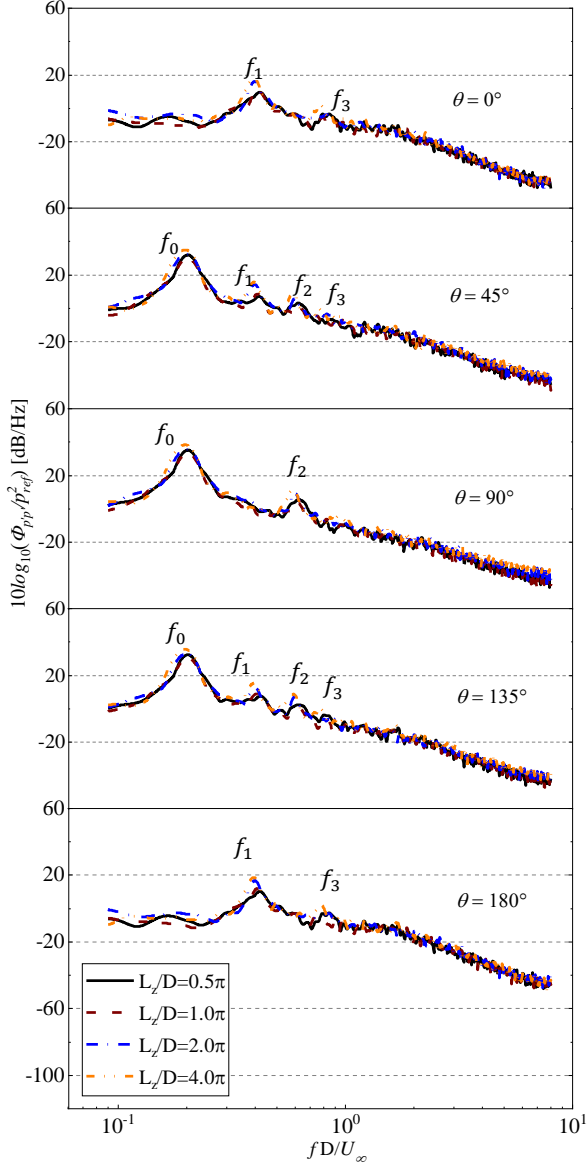


FIG. 17. Spanwise length corrected PSD from the cases with different spanwise lengths at different angles.

damental vortex shedding frequency ( $f_0$ ). Yet, at  $\theta = 0^\circ$  and  $\theta = 180^\circ$ , the peaks at the fundamental frequency ( $f_0$ ) and the second harmonic ( $f_2$ ) vanish, whereas the tonal peaks are at the first harmonic ( $f_1$ ) and the third harmonic ( $f_3$ ). Similarly, the first harmonic ( $f_1$ ) and third harmonic ( $f_3$ ) peaks vanish at  $\theta = 90^\circ$ . The fundamental frequency peak, first and second harmonic peaks occur at  $\theta = 45^\circ$  and  $\theta = 135^\circ$  in all cases. Compared with other cases, the  $4\pi D$  case could well capture the peak at the third harmonic ( $f_3$ ) at  $\theta = 45^\circ$  and  $\theta = 135^\circ$ .

Figure 18 shows the acoustic pressure PSD of the case with  $L_z=4\pi D$  at different polar angles. Compared with the near-field results in section III A 1, the broadband energy contents of the acoustic pressure PSD at different angles are consistent with each other in the frequency range of  $St > 0.9$ , which

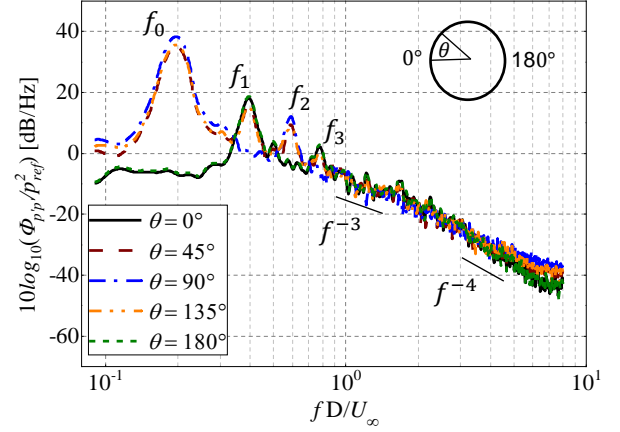


FIG. 18. Far-field acoustic PSD from the case with  $L_z=4\pi D$  at different angles.

means the high-frequency pressure fluctuation dissipates in a similar way in the far-field. The slopes keep the value of  $f^{-3}$  from  $St = 0.9$  to  $St = 2$  and change to  $f^{-4}$  when  $St$  is greater than 2. For the tonal components, the dipole distribution shows a symmetric feature about  $\theta = 90^\circ$ , that the peaks of  $\theta = 0^\circ$  and  $\theta = 45^\circ$  are almost the same with those of  $\theta = 180^\circ$  and  $\theta = 135^\circ$ , respectively. The magnitude of the dominant peak experiences an increase from  $\theta = 45^\circ$  to  $\theta = 90^\circ$ , which is directly above the cylinder and the lift fluctuation affects the most. Then, the peak value decreases from  $\theta = 90^\circ$  to  $\theta = 135^\circ$ . The tonal peak at the fundamental vortex shedding frequency of  $\theta = 90^\circ$  is higher than that of  $\theta = 45^\circ$  and  $\theta = 135^\circ$  by about 4 dB/Hz.

## 2. Validation with experimental far-field noise measurements

### 2.1 Spanwise length-velocity corrected PSD

The in-house experiments have a different set of conditions from the numerical simulations, and hence, both the spanwise length and the velocity need to be corrected. While the spanwise length is corrected through Kato's method<sup>21</sup>, the velocity is corrected through:

$$\begin{cases} \Delta\text{PSD} = 10 \log_{10}(D/D_s) \\ \Delta\text{PSD} = 60 \log_{10}(U/U_s) \\ \Delta\text{PSD} = 20 \log_{10}(r_s/r). \end{cases} \quad (11)$$

based on the acoustic pressure calculation method established by Phillips<sup>59</sup>,

$$\overline{p^2} \simeq 0.27 \cos^2 \theta \frac{\rho U^6 S^2 L D}{c^2 r^2}, \quad (12)$$

where  $\theta$  is the angle between the direction of the observation point and the streamwise direction.  $L$  is the length of the cylinder.  $D$  is the diameter of the cylinder, and  $r$  is the distance between the sound source and the observer. Finally,  $\rho$  is the density,  $c$  is the sound velocity and  $S$  is the strength of the

vortices. Besides, the cylinder diameter  $D$  and the distance  $r$  could also be corrected. The subscript  $s$  represents the prediction from numerical simulations.

To compare directly with the experimental results, both the spanwise length and velocity corrections are applied to the simulation results. Recall that the cylinder used in the experiments has a spanwise length of  $L_z = 25D$  and moreover, results from  $U_\infty = 30$  m/s were selected so that the far-field noise from the cylinder was notably higher than that of the background. The spanwise length-velocity corrected PSD is shown in Fig. 19, where the in-house experimental data at  $45^\circ$  and  $90^\circ$  are presented for comparison. Compared to the spanwise length corrected PSD, the magnitude of the spanwise length-velocity corrected PSD increases due to the higher ‘corrected’ velocity. The experimental results show the tonal peak at fundamental vortex shedding frequency with a difference of about 7.76 dB/Hz compared to the simulated results. The fundamental vortex shedding frequency of experiments deviates slightly from the theoretical value of  $St = 0.2$ . At the first, second and third harmonics, the simulated results show more obvious peaks than the experimental ones. The tonal peaks captured by the  $4\pi D$  case are more obvious than its counterparts, especially at harmonics.

In summary, the CFD/acoustic analogy hybrid method shows a good ability to predict the acoustic pressure, and the tonal components of PSD are well captured. The spanwise length correction method of Kato works well to eliminate the difference in the predicted noise magnitudes of the cases with different spanwise lengths. The spanwise length-velocity corrected PSD is comparable to the experimental results, both for the tonal and broadband components.

## 2.2 Comparison of Octave bands with literature data

The octave band could give sufficient information about the spectra with the octave band frequency, which is distinguishable and comparable. The spanwise length and velocity corrections of Eqs. 10 and 11 are applied to both the simulation results and the in-house experimental results for the comparison with the literature data from<sup>24,60</sup>. In the studies of<sup>24,60</sup>, the observer was located at  $\theta = 90^\circ$  with a distance between the sound source and the observer  $r = 5m$ . The cylinder diameter and the spanwise length were 0.05 m and 0.15 m respectively, and the streamwise speed was 30 m/s. Also, the same sampling duration of 0.5 s is used to compute the narrowband acoustic pressure PSD from the present simulation and experimental results. Then, the narrowbands are integrated into one-sixth octave bands, shown in Fig. 20.

The tonal peaks at  $St = 0.2$  and  $St = 0.6$  are well captured for all cases, consistent with the results in Fig. 17. Good agreements are found for the peak values at the fundamental vortex shedding frequency and the differences in the peak values are within 6.59 dB. For the second harmonic peak, the deviation of the far-field SPL is up to about 8.39 dB. The in-house experimental data matches well with the literature data, except for the values at  $St < 0.1$ . The SPL value of the simulations is higher than that of the experiments in the range of  $0.2 < St < 0.3$ , because the spanwise length of the computational domain is smaller than that of the experimental

model, and the captured flow structures are more correlated, contributing to higher predicted SPL. The octave bands are within an acceptable range, and the method used in this paper shows a good ability to predict the far-field noise of the cylinders.

## 3. Far-field noise directivity

Figure 21 shows the far-field noise directivities for the cases with different spanwise lengths. The OASPL is presented in Fig. 21 (a), calculated with regard to the frequency range from  $St = 0.09$  to  $St = 8$ . The OASPL shows a dipole pattern that is symmetric about the streamwise direction and the vertical direction, and the OASPL values at  $\theta = 90^\circ$  and  $\theta = 270^\circ$  are the maximum while the values at  $\theta = 0^\circ$  and  $\theta = 180^\circ$  are the minimum. The reason is that the flow separation happens in the upper and lower sides of the cylinder, and the fluctuation in the vertical direction related to the lift is stronger than that in the streamwise direction related to the drag. The difference in the OASPL between the cases with different spanwise lengths is within 5.4 dB. The difference between the OASPL values at  $\theta = 90^\circ$  and  $\theta = 0^\circ$  is approximately 18 dB, close to the results of<sup>24</sup> in the subcritical Reynolds number range.

Figure 21 (b-d) show the tonal peaks directivity of the spanwise length-velocity corrected PSD. For the fundamental vortex shedding frequency and the second harmonic, a dipole pattern occurs with the maximum values aligned normal to the stream, which is the same with the OAPSL distribution. For the first harmonic, the maximum SPL is aligned parallel to the stream. This phenomenon is consistent with the result of<sup>61</sup> that the total sound field is the superposition of a dipole sound field aligned normal to the stream and a dipole field aligned parallel to the stream.

The difference between the maxima and the minima is up to 45 dB at the fundamental vortex shedding frequency due to the dipole nature of the major tonal peak. The difference in magnitude decreases at the first and second harmonics. The dipole behaviors are better captured for the  $2\pi D$  and  $4\pi D$  cases than the  $0.5\pi D$  and  $\pi D$  cases. Also, at higher harmonics, the PSD values are larger for the  $2\pi D$  and  $4\pi D$  cases than that of the  $0.5\pi D$  and  $\pi D$  cases in the lift direction, which means the case with longer spanwise length could capture the harmonic peaks better.

## IV. Conclusions

The aerodynamic noise of flow past a cylinder at  $Re = 10,000$  is investigated by a hybrid method of LES and the FW-H acoustic analogy. Four spanwise lengths are chosen:  $0.5\pi D$ ,  $\pi D$ ,  $2\pi D$ ,  $4\pi D$ . For all cases, the pressure coefficient  $C_p$  value and the time-averaged streamwise velocity are validated well with the in-house experimental data and the literature. The major conclusions are as following:

(1) The near-field pressure PSD and velocity PSD are well predicted and their values and changing trends are acceptable. Different spanwise lengths have very limited impact on the

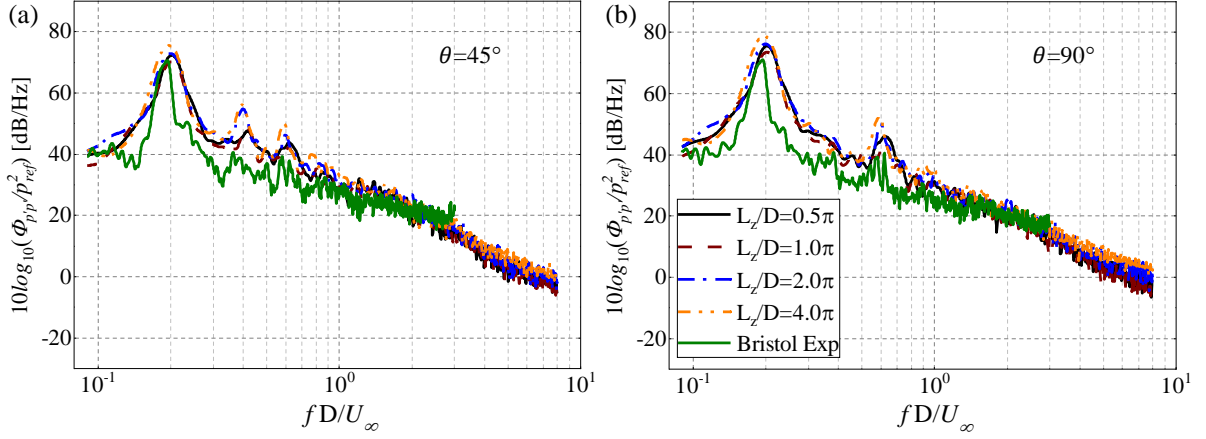


FIG. 19. Spanwise length-velocity corrected PSD from the cases with different spanwise lengths at (a)  $\theta = 45^\circ$  and (b)  $\theta = 90^\circ$ .

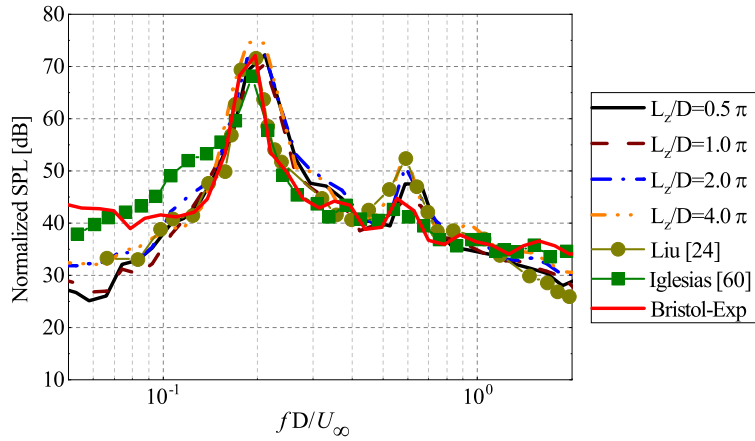


FIG. 20. Normalized 1/6 octave band noise spectrum calculated from the spanwise length-velocity corrected PSD of the cases with different spanwise lengths at  $\theta = 90^\circ$ .

surface pressure and velocity PSD at different spanwise locations. However, the  $0.5\pi D$  overpredicts the spanwise pressure coherence value and shows a much lower coherence decay rate than the cases with longer spanwise lengths, which has strong implications for the prediction of the far-field noise.

(2) Proper Orthogonal Decomposition has been performed on the three-dimensional flow field in the near-wake. The most energetic flow structure of flow past a cylinder is the vortex shedding. The highly correlated (two-dimensional) vortex shedding is included in the first and second POD modes. For the third and fourth POD modes, the cases with spanwise lengths from  $\pi D$  to  $4\pi D$  still exhibit flow structures associated with the fundamental vortex shedding, but with clear spanwise variations (*i.e.*, more three-dimensional). The third mode of the  $0.5\pi D$  case shows relatively higher coherent flow structures than other cases, but not related to the fundamental vortex shedding frequency.

(3) The hybrid CFD/acoustic analogy method shows a good ability to predict the acoustic pressure, and the tonal components of far-field noise are well captured. The simulation results and experimental results are consistent with the litera-

ture data, indicating the good noise prediction capability of the method in this study. The correction method for the spanwise length, taking into account the spanwise pressure coherence, performs well in the subcritical Reynolds number range. After correction, the predicted far-field noise from different spanwise length cases collapses onto each other well; nevertheless, the  $4\pi D$  is able to better capture the higher harmonics. The results comparison reaffirms that the coherence length plays a crucial role in the spanwise length correction. Such a correction method warrants further investigation for critical and super-critical flow regimes in the future.

(4) All four cases show reasonable far-field noise directivities. The cases with spanwise lengths of  $2\pi D$  and  $4\pi D$  perform better with more clearly defined dipole patterns, especially for the directivities of SPL peaks at the first and second harmonics.

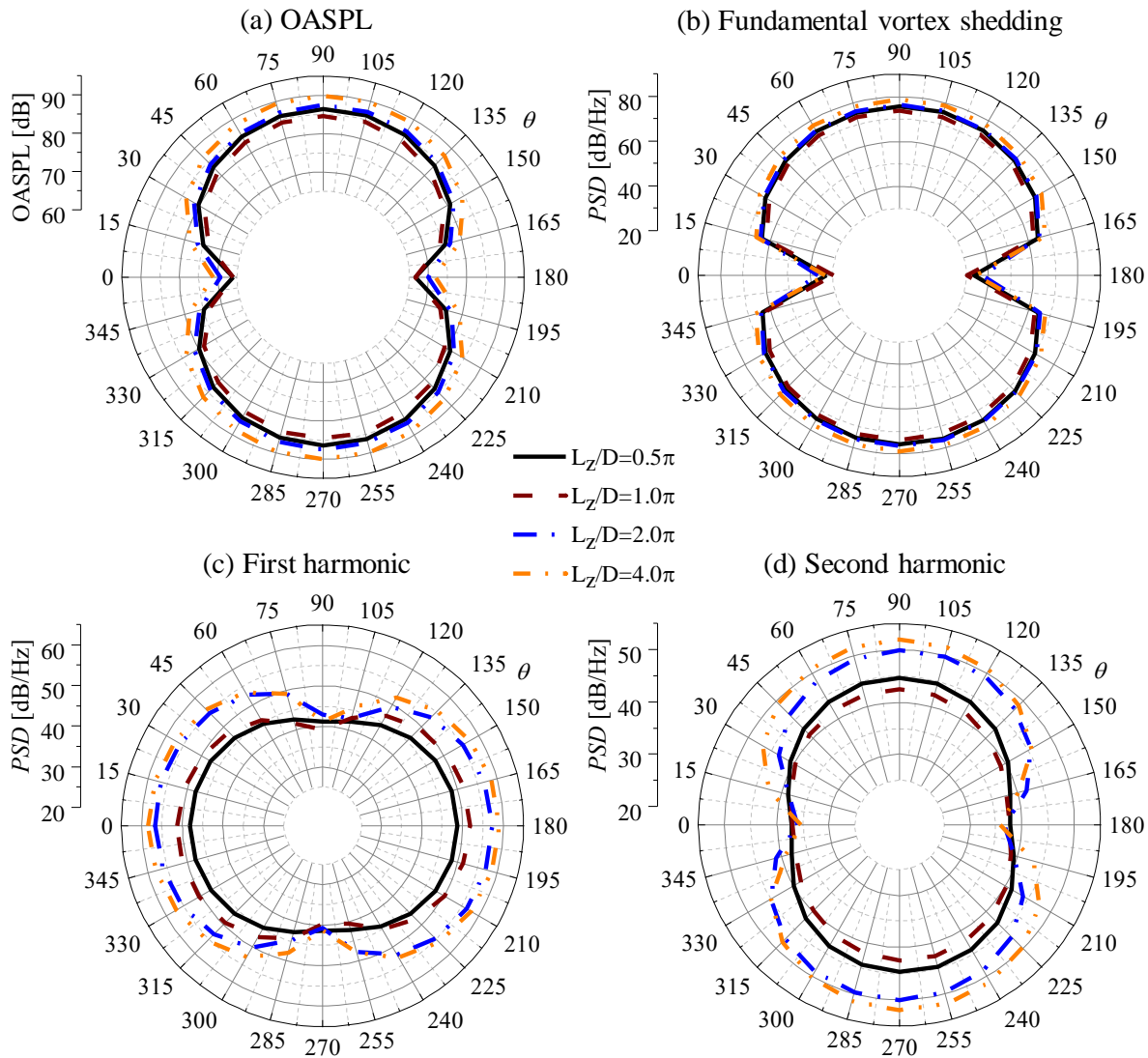


FIG. 21. Far-field noise directivities calculated from the spanwise length-velocity corrected PSD of the cases with different spanwise lengths, including (a) OASPL, and at (b) fundamental vortex shedding frequency, (c) first harmonic, (d) second harmonic.

### Acknowledgements

The authors acknowledge the Advanced Computing Research Center (ACRC) of the University of Bristol. The first author's PhD grant is funded by the China Scholarship Council (CSC)-University of Bristol (UoB) PhD Scholarship (Funding number: CSC201906230299).

**Declaration:** The authors declare no conflict of interest for the present work.

<sup>1</sup>E. Houghton and P. Carpenter, eds., "Chapter 3 - viscous flow and boundary layers," in *Aerodynamics for Engineering Students* (Todd Green, 2017) Chap. 3, pp. 173–180.

<sup>2</sup>C. Zhang, M. Sanjosé, and S. Moreau, "Aeolian noise of a cylinder in the critical regime," *The Journal of the Acoustical Society of America* **146**, 1404–1415 (2019).

<sup>3</sup>S.-E. Kim, "Large Eddy Simulation of turbulent flow past a circular cylinder in subcritical regime," in *44th AIAA aerospace sciences meeting and exhibit* (Reno, Nevada, 2006) pp. 2006–1418.

<sup>4</sup>M. Breuer, "Large Eddy Simulation of the subcritical flow past a circular cylinder: numerical and modeling aspects," *International Journal for Numerical Methods in Fluids* **28**, 1281–1302 (1998).

<sup>5</sup>M. Breuer, "Numerical and modeling influences on Large Eddy Simulations for the flow past a circular cylinder," *International Journal of Heat and Fluid Flow* **19**, 512–521 (1998).

<sup>6</sup>D. Lysenko, I. Ertesvåg, and K. Rian, "Large Eddy Simulation of the flow over a circular cylinder at Reynolds number 3900 using the OpenFOAM toolbox," *Flow, Turbulence and Combustion* **89**, 491–518 (2012).

<sup>7</sup>D. Lysenko, I. Ertesvåg, and K. Rian, "Large Eddy Simulation of the flow over a circular cylinder at Reynolds number  $2 \times 10^4$ ," *Flow, turbulence and combustion* **92**, 673–698 (2014).

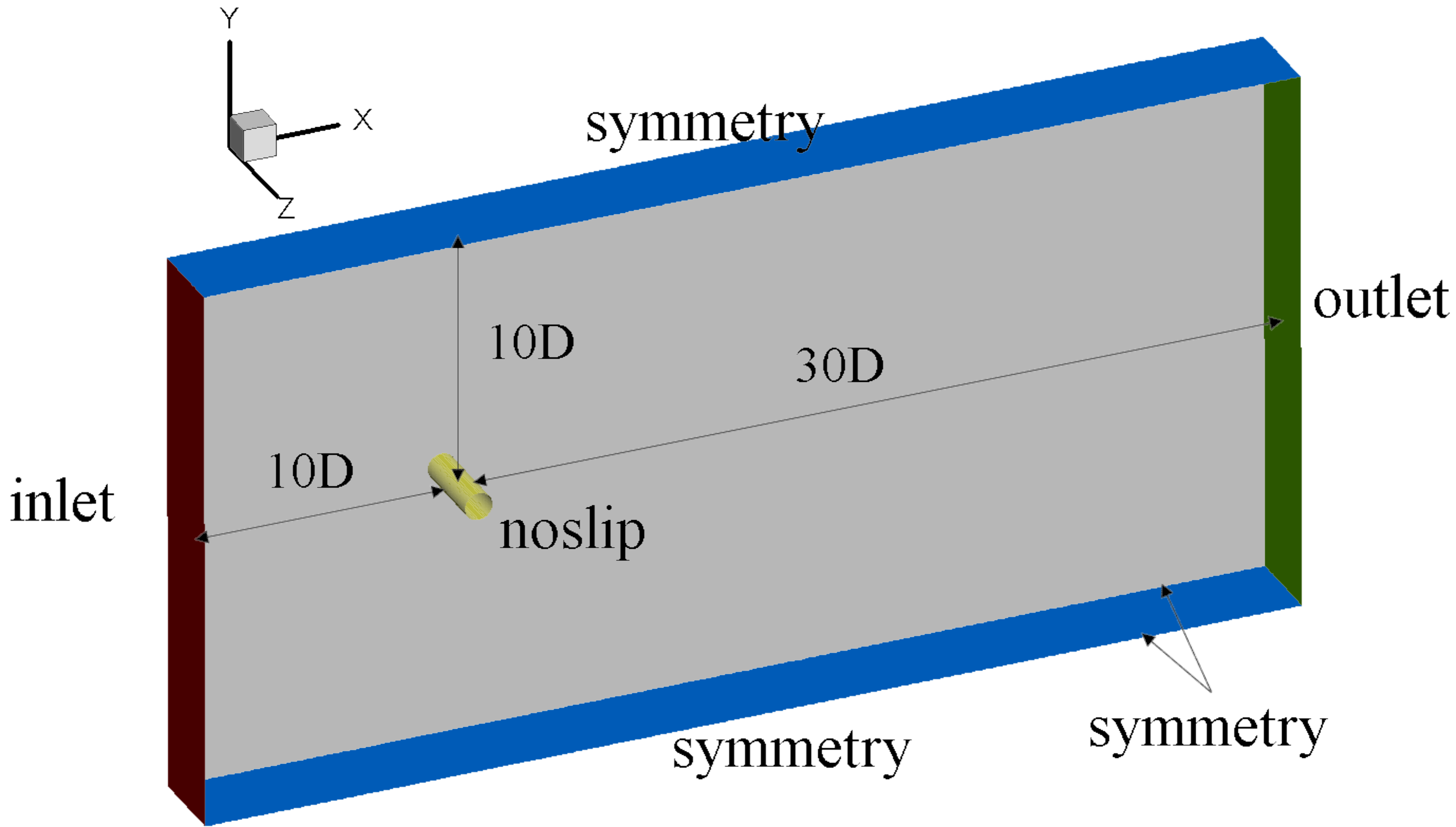
<sup>8</sup>M. Young and A. Ooi, "Comparative assessment of LES and URANS for flow over a cylinder at a Reynolds number of 3900," in *16th Australasian Fluid Mechanics Conference* (Gold Coast, Australia, 2007) pp. 1063–1070.

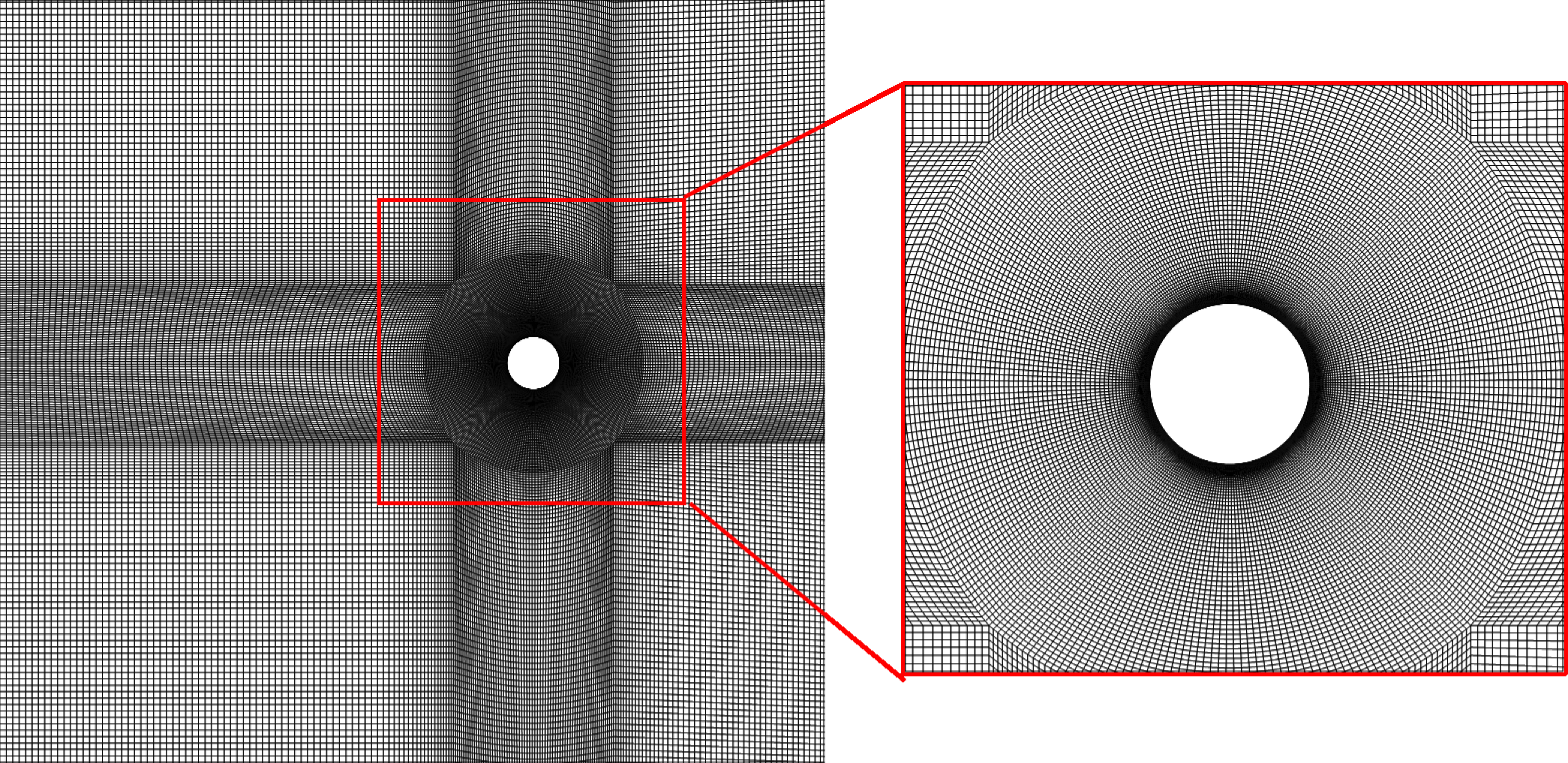
<sup>9</sup>S. Wornom, H. Ouvrard, M. Salvetti, B. Koobus, and A. Dervieux, "Variational multiscale Large Eddy Simulations of the flow past a circular cylinder,"

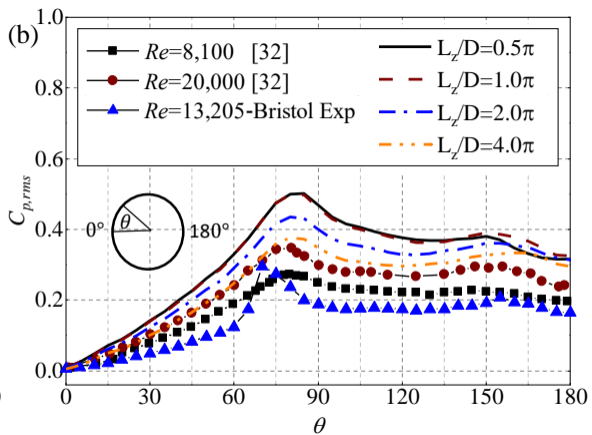
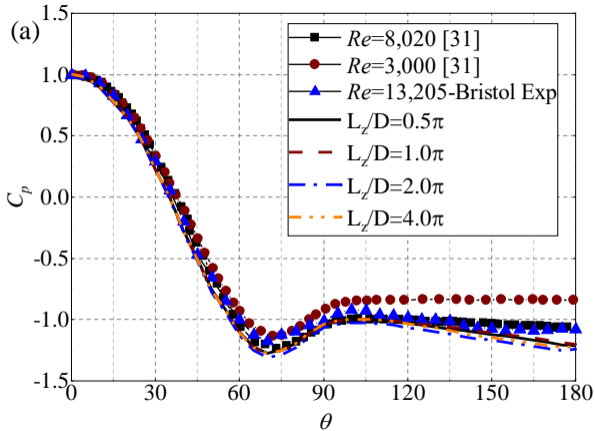
- der: Reynolds number effects,” *Computers & Fluids* **47**, 44–50 (2011).
- <sup>10</sup>C. Zhang, M. Sanjosé, and S. Moreau, “Wall-modeled Large Eddy Simulation with adverse pressure gradients: Application to bluff bodies,” in *Proceeding of 26th Annual Conference of the CFD Society of Canada* (2018).
  - <sup>11</sup>C. Zhang, S. Moreau, and M. Sanjosé, “Turbulent flow and noise sources on a circular cylinder in the critical regime,” *AIP Advances* **9**, 085009 (2019).
  - <sup>12</sup>J. Franke and W. Frank, “Large Eddy Simulation of the flow past a circular cylinder at  $Re_D=3900$ ,” *Journal of wind engineering and industrial aerodynamics* **90**, 1191–1206 (2002).
  - <sup>13</sup>N. Khan, Z. Ibrahim, A. Badry, J. Mohammed, and M. F. Javed, “Numerical investigation of flow around cylinder at Reynolds number= 3900 with Large Eddy Simulation technique: effect of spanwise length and mesh resolution,” *Proceedings of the Institution of Mechanical Engineers, Part M: Journal of Engineering for the Maritime Environment* **233**, 417–427 (2019).
  - <sup>14</sup>M. Breuer, “A challenging test case for Large Eddy Simulation: high Reynolds number circular cylinder flow,” *International Journal of Heat and Fluid Flow* **21**, 648–654 (2000).
  - <sup>15</sup>M. Prsic, M. Ong, B. Pettersen, and D. Myrhaug, “Large Eddy Simulations of flow around a smooth circular cylinder in a uniform current in the subcritical flow regime,” *Ocean Engineering* **77**, 61–73 (2014).
  - <sup>16</sup>Z. Nitzkorski and K. Mahesh, “A dynamic end cap technique for sound computation using the Ffowcs Williams and Hawkings equations,” *Physics of Fluids* **26**, 115101 (2014).
  - <sup>17</sup>M. Cianferra, S. Ianniello, and V. Armenio, “Assessment of methodologies for the solution of the Ffowcs Williams and Hawkings equation using LES of incompressible single-phase flow around a finite-size square cylinder,” *Journal of Sound and Vibration* **453**, 1–24 (2019).
  - <sup>18</sup>Y. Zhang, Y. Xiao, R. Liu, and H. Chen, “Aeroacoustic prediction based on Large-Eddy Simulation and the Ffowcs Williams–Hawkings equation,” *Advances in Aerodynamics* **4**, 1–18 (2022).
  - <sup>19</sup>K. Karthik, S. Vengadesan, and S. Bhattacharyya, “Prediction of flow induced sound generated by cross flow past finite length circular cylinders,” *The Journal of the Acoustical Society of America* **143**, 260–270 (2018).
  - <sup>20</sup>R. Orselli, J. Meneghini, and F. Saltara, “Two and three-dimensional simulation of sound generated by flow around a circular cylinder,” in *15th AIAA/CEAS aeroacoustics conference (30th AIAA aeroacoustics conference)* (Miami, Florida, 2009) p. 3270.
  - <sup>21</sup>C. Kato, A. Iida, Y. Takano, H. Fujita, and M. Ikegawa, “Numerical prediction of aerodynamic noise radiated from low Mach number turbulent wake,” in *31st Aerospace Sciences Meeting* (Reno, NV, 1993) p. 145.
  - <sup>22</sup>J. Revell, R. Prydz, and A. Hays, “Experimental study of aerodynamic noise vs drag relationships for circular cylinders,” *AIAA Journal* **16**, 889–897 (1978).
  - <sup>23</sup>J. Jacob and S. K. Bhattacharya, “Aerodynamic noise from long circular and non-circular cylinders using Large Eddy Simulations,” *International Journal of Aeroacoustics* **21**, 142–167 (2022).
  - <sup>24</sup>X. Liu, D. Thompson, and Z. Hu, “Numerical investigation of aerodynamic noise generated by circular cylinders in cross-flow at Reynolds numbers in the upper subcritical and critical regimes,” *International Journal of Aeroacoustics* **18**, 470–495 (2019).
  - <sup>25</sup>B. Chen, X. Yang, G. Chen, X. Tang, J. Ding, and P. Weng, “Numerical study on the flow and noise control mechanism of wavy cylinder,” *Physics of Fluids* **34**, 036108 (2022).
  - <sup>26</sup>S. Chu, C. Xia, H. Wang, Y. Fan, and Z. Yang, “Three-dimensional spectral Proper Orthogonal Decomposition analyses of the turbulent flow around a seal-vibrissa-shaped cylinder,” *Physics of Fluids* **33**, 025106–1–16 (2021).
  - <sup>27</sup>H. Kim and H. S. Yoon, “Effect of the orientation of the harbor seal vibrissa based biomimetic cylinder on hydrodynamic forces and vortex induced frequency,” *AIP Advances* **7**, 105015 (2017).
  - <sup>28</sup>A. Epikhin, I. Evdokimov, M. Kraposhin, M. Kalugin, and S. Strijhak, “Development of a dynamic library for computational aeroacoustics applications using the OpenFOAM open source package,” *Procedia Computer Science* **66**, 150–157 (2015).
  - <sup>29</sup>G. Rosetti, G. Vaz, and A. Fujarra, “URANS calculations for smooth circular cylinder flow in a wide range of Reynolds numbers: solution verification and validation,” *Journal of Fluids Engineering* **134** (2012).
  - <sup>30</sup>C. J. Greenshields, ed., “Numerical schemes,” in *OpenFOAM user guide-version 6* (OpenFOAM Foundation Ltd, 2018) Chap. 4.4, pp. 118–132.
  - <sup>31</sup>C. Norberg, “Effects of Reynolds number and a low-intensity freestream turbulence on the flow around a circular cylinder,” *Tech. Rep. ISSN 02809265* (Chalmers University, Goteborg, Sweden, Technological Publications, 1987).
  - <sup>32</sup>C. Norberg, “Fluctuating lift on a circular cylinder: review and new measurements,” *Journal of Fluids and Structures* **17**, 57–96 (2003).
  - <sup>33</sup>A. Mani, P. Moin, and M. Wang, “Computational study of optical distortions by separated shear layers and turbulent wakes,” *Journal of Fluid Mechanics* **625**, 273–298 (2009).
  - <sup>34</sup>S. Sharma, T. F. Geyer, and E. Arcondoulis, “Effect of coating thickness on aerodynamic noise reduction by porous-coated cylinders,” in *28th AIAA/CEAS Aeroacoustics 2022 Conference* (2022) p. 2889.
  - <sup>35</sup>C. Wagner, T. Hüttele, and P. Sagaut, “Chapter 5 - numerical method,” in *Large Eddy Simulation for Aeroacoustics* (Cambridge: Cambridge University Press, 2006) Chap. 5, pp. 267–237.
  - <sup>36</sup>M. Lighthill, “On sound generated aerodynamically I. General theory,” *Proceedings of the Royal Society of London. Series A. Mathematical and Physical Sciences* **211**, 564–587 (1952).
  - <sup>37</sup>M. Lighthill, “On sound generated aerodynamically II. Turbulence as a source of sound,” *Proceedings of the Royal Society of London. Series A. Mathematical and Physical Sciences* **222**, 1–32 (1954).
  - <sup>38</sup>N. Curle, “The influence of solid boundaries upon aerodynamic sound,” *Proceedings of the Royal Society of London. Series A. Mathematical and Physical Sciences* **231**, 505–514 (1955).
  - <sup>39</sup>J. Williams and D. Hawkings, “Sound generation by turbulence and surfaces in arbitrary motion,” *Philosophical Transactions of the Royal Society of London. Series A, Mathematical and Physical Sciences* **264**, 321–342 (1969).
  - <sup>40</sup>F. Farassat, “Derivation of Formulations 1 and 1A of Farassat,” *Tech. Rep. NASA/TM-2007-214853* (Langley Research Center, Hampton, Virginia, 2007).
  - <sup>41</sup>G. Brès, F. Pérot, and D. Freed, “A Ffowcs Williams-Hawkings solver for Lattice-Boltzmann based computational aeroacoustics,” in *16th AIAA/CEAS aeroacoustics conference* (Stockholm, Sweden, 2010) p. 3711.
  - <sup>42</sup>Y. Mayer, H. Jawahar, M. Szöke, S. Ali, and M. Azarpeyvand, “Design and performance of an aeroacoustic wind tunnel facility at the University of Bristol,” *Applied Acoustics* **155**, 358–370 (2019).
  - <sup>43</sup>R. Maryami, S. A. Showkat Ali, M. Azarpeyvand, and A. Afshari, “Turbulent flow interaction with a circular cylinder,” *Physics of Fluids* **32**, 015105 (2020).
  - <sup>44</sup>R. Maryami, M. Azarpeyvand, A. Dehghan, and A. Afshari, “An experimental investigation of the surface pressure fluctuations for round cylinders,” *Journal of Fluids Engineering* **141** (2019).
  - <sup>45</sup>G. Chen, X. Liu, B. Zang, and M. Azarpeyvand, “The effect of the splitter plate on the aeolian tone mitigation,” in *28th AIAA/CEAS Aeroacoustics 2022 Conference* (2022) pp. 3094–1–11.
  - <sup>46</sup>X. Liu, G. Chen, B. Zang, and M. Azarpeyvand, “An experimental study of aerodynamic noise of the wavy and vibrissa shaped cylinders,” in *28th AIAA/CEAS Aeroacoustics 2022 Conference* (2022) pp. 2982–1–15.
  - <sup>47</sup>C. Norberg and B. Sunden, “Turbulence and Reynolds number effects on the flow and fluid forces on a single cylinder in cross flow,” *Journal of Fluids and Structures* **1**, 337–357 (1987).
  - <sup>48</sup>A. Prasad and C. Williamson, “The instability of the shear layer separating from a bluff body,” *Journal of Fluid Mechanics* **333**, 375–402 (1997).
  - <sup>49</sup>X. Ma, *Hierarchical Galerkin and non-linear Galerkin models for laminar and turbulent wakes*, Ph.D. thesis, Brown University (2001).
  - <sup>50</sup>T. Iliescu and Z. Wang, “Variational multiscale Proper Orthogonal Decomposition: Navier-Stokes equations,” *Numerical Methods for Partial Differential Equations* **30**, 641–663 (2014).
  - <sup>51</sup>M. Janocha, L. Fabricius, G. Yin, and M. Ong, “Three-dimensional Large Eddy Simulations and Proper Orthogonal Decomposition analysis of flow around a flexibly supported circular cylinder,” *Journal of Offshore Mechanics and Arctic Engineering* **144**, 060902–1–22 (2022).
  - <sup>52</sup>L. Sirovich, “Turbulence and the dynamics of coherent structures. I. Coherent structures,” *Quarterly of Applied Mathematics* **45**, 561–571 (1987).
  - <sup>53</sup>R. Perrin, M. Braza, E. Cid, S. Cazin, P. Patrick, C. Mockett, T. Reimann, and F. Thiele, “Coherent and turbulent process analysis in the flow past a circular cylinder at high Reynolds number,” *Journal of Fluids and Structures* **24**, 1313–1325 (2008).

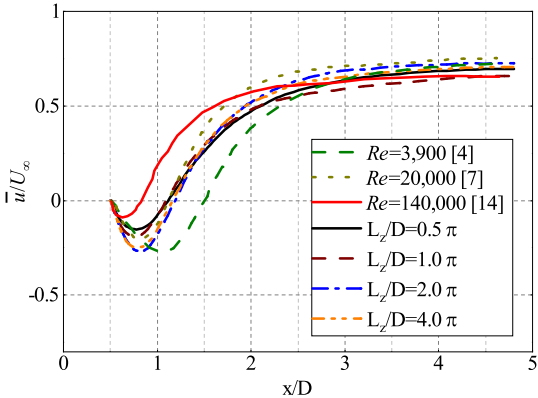
- <sup>54</sup>J. Weiss, “A tutorial on the Proper Orthogonal Decomposition,” in *2019 AIAA Aviation Forum* (Dallas, Texas, United States, 2019) pp. 1–21.
- <sup>55</sup>L. Feng, J. Wang, and C. Pan, “Proper Orthogonal Decomposition analysis of vortex dynamics of a circular cylinder under synthetic jet control,” *Physics of Fluids* **23**, 014106 (2011).
- <sup>56</sup>B. Noack, K. Afanasiev, M. Morzyński, G. Tadmor, and F. Thiele, “A hierarchy of low-dimensional models for the transient and post-transient cylinder wake,” *Journal of Fluid Mechanics* **497**, 335–363 (2003).
- <sup>57</sup>L. Kourentis and E. Konstantinidis, “Uncovering large-scale coherent structures in natural and forced turbulent wakes by combining PIV, POD, and FTLE,” *Experiments in Fluids* **52**, 749–763 (2012).
- <sup>58</sup>J. Seo and Y.J. Moon, “Aerodynamic noise prediction for long-span bodies,” *Journal of Sound and Vibration* **306**, 564–579 (2007).
- <sup>59</sup>O. Phillips, “The intensity of Aeolian tones,” *Journal of Fluid Mechanics* **1**, 607–624 (1956).
- <sup>60</sup>E. Iglesias, D. Thompson, and M. Smith, “Experimental study of the aerodynamic noise radiated by cylinders with different cross-sections and yaw angles,” *Journal of Sound and Vibration* **361**, 108–129 (2016).
- <sup>61</sup>J. Hardin and S. Lamkin, “Aeroacoustic Computation of Cylinder Wake Flow,” *AIAA journal* **22**, 51–57 (1984).

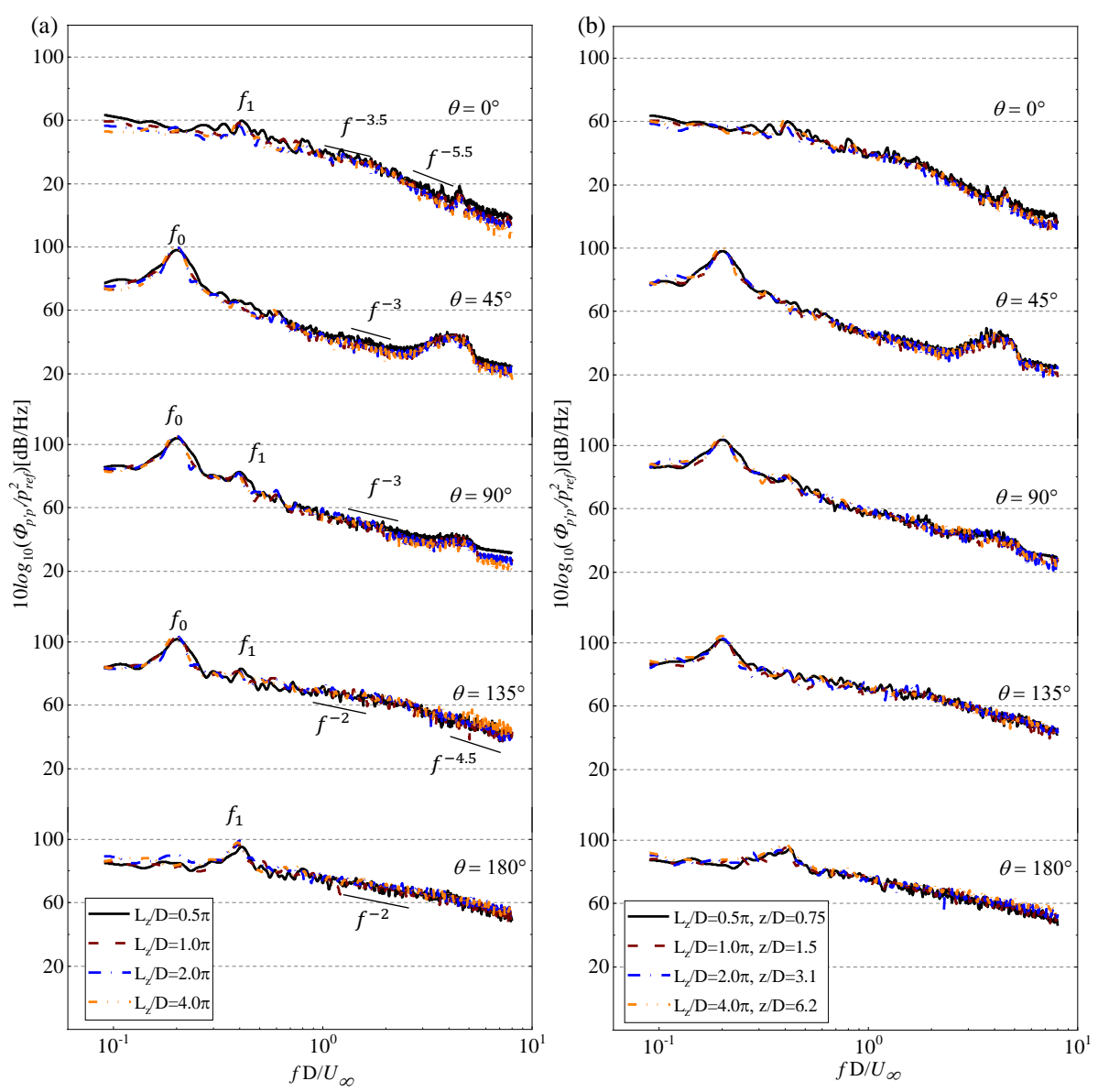


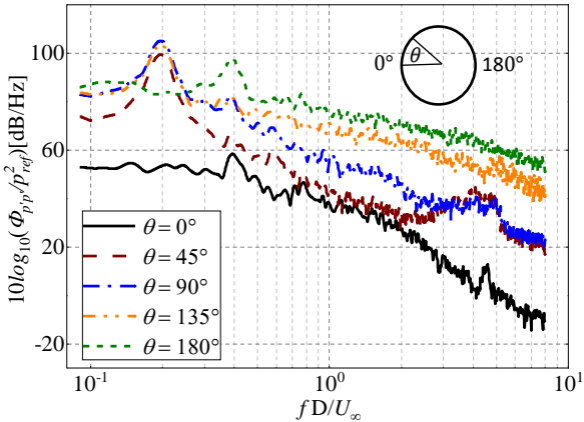


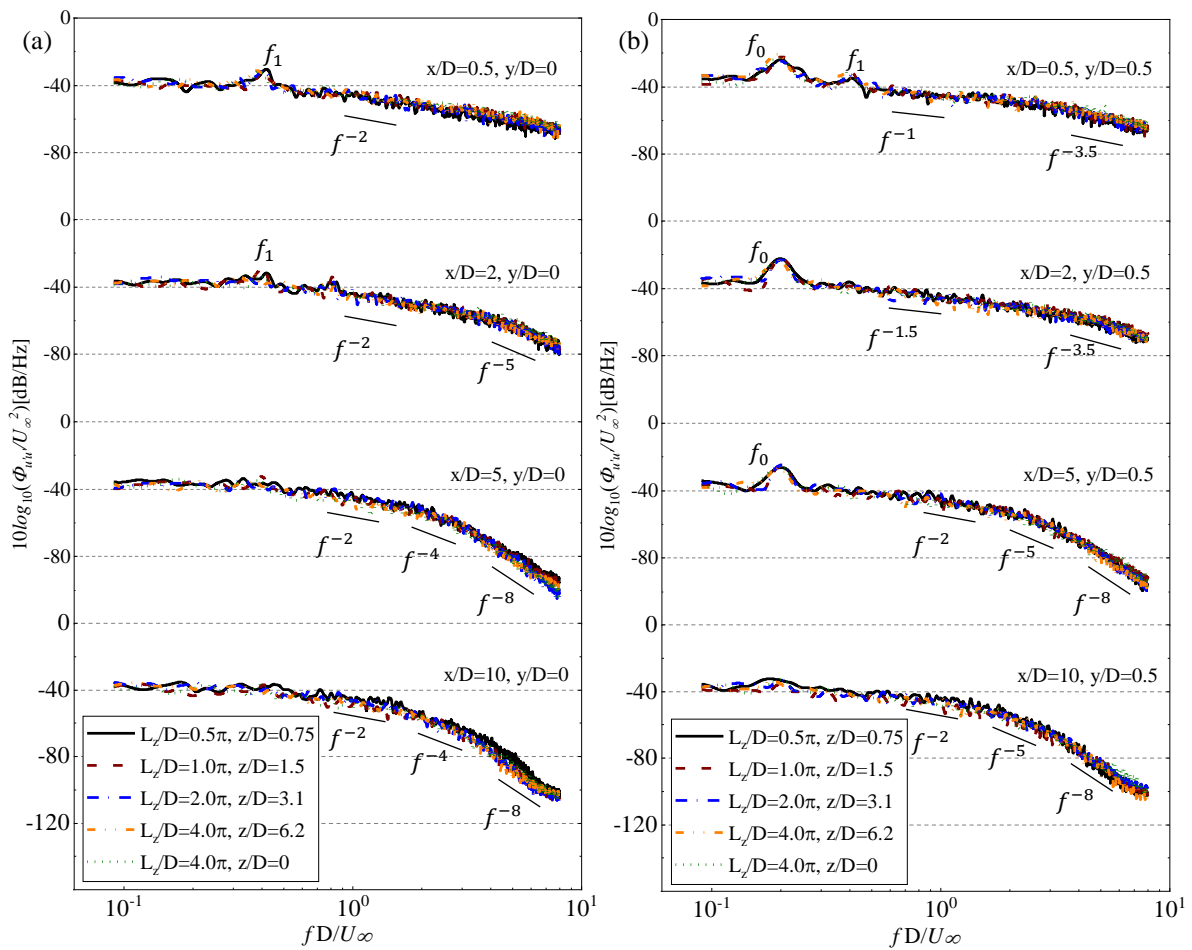


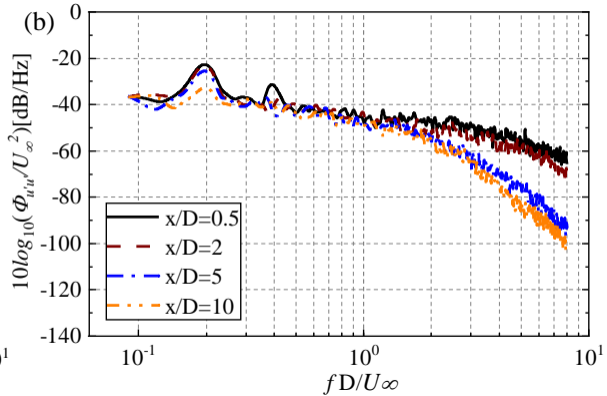
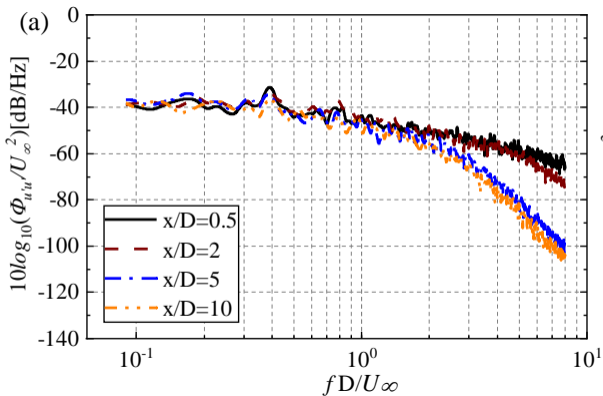




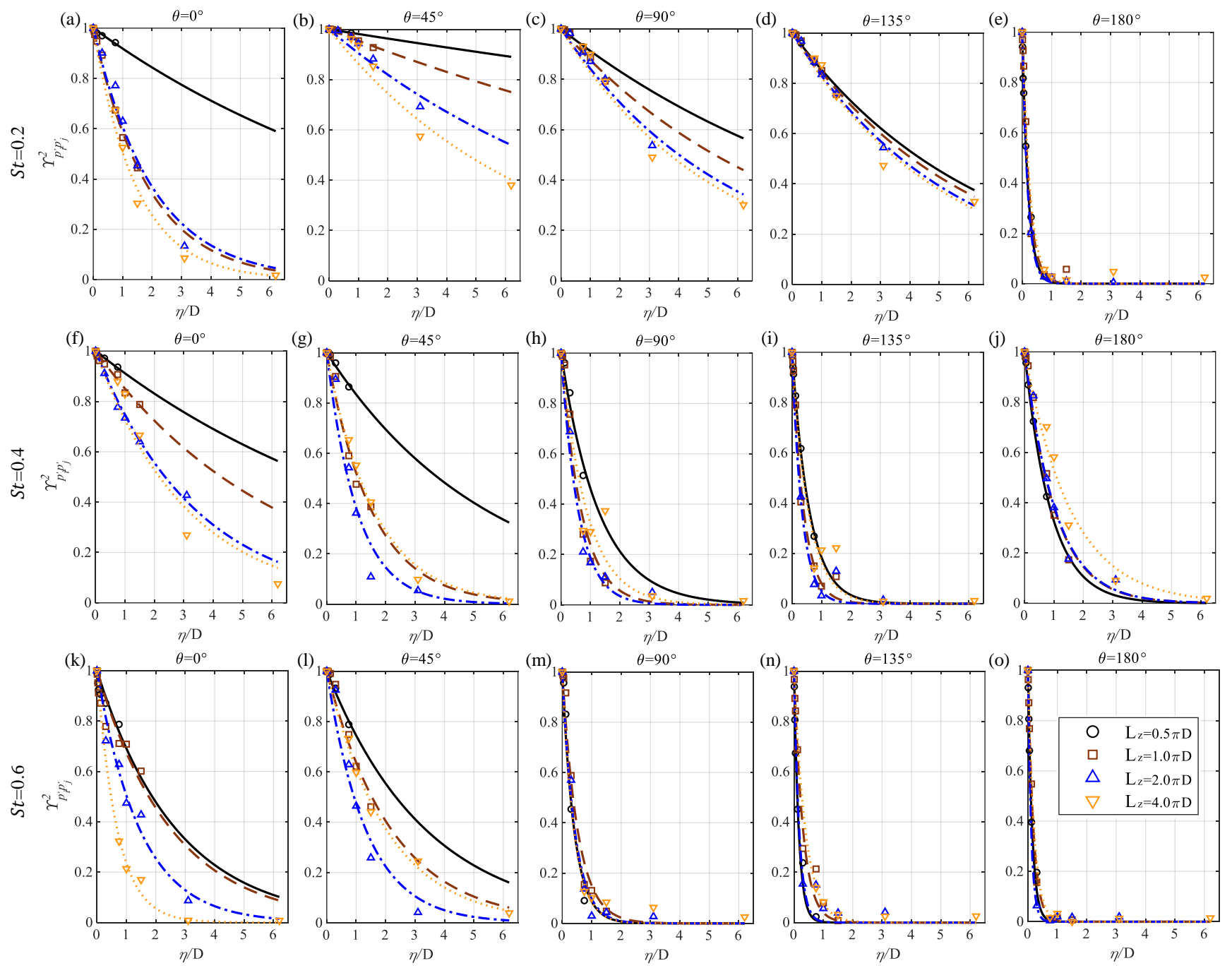


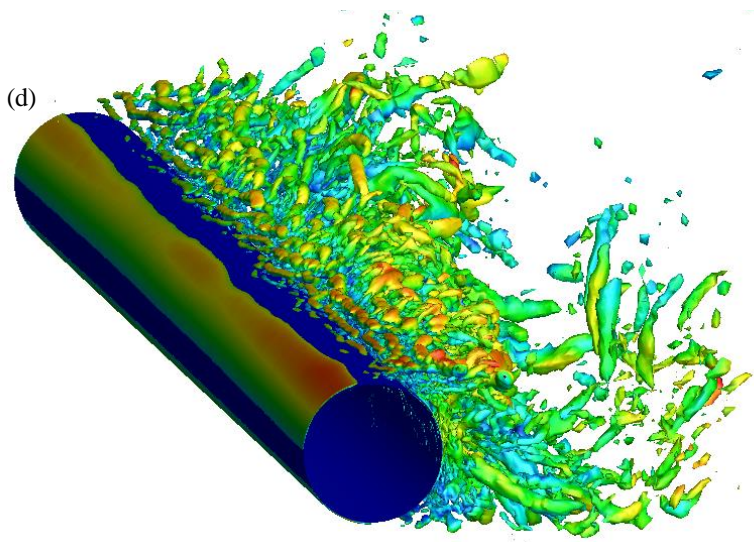
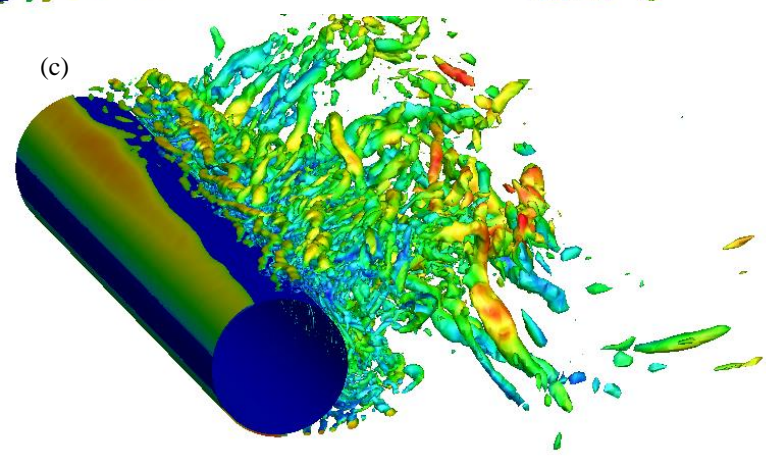
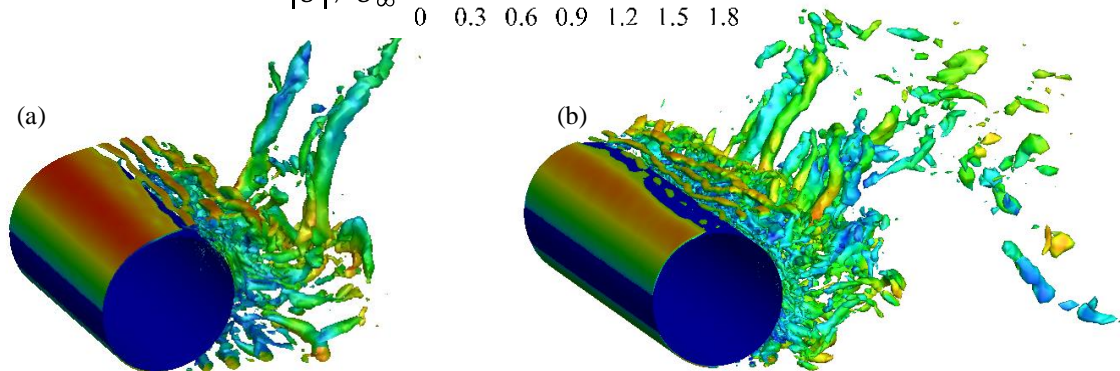
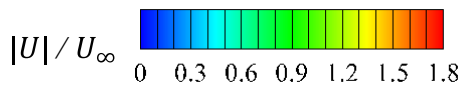


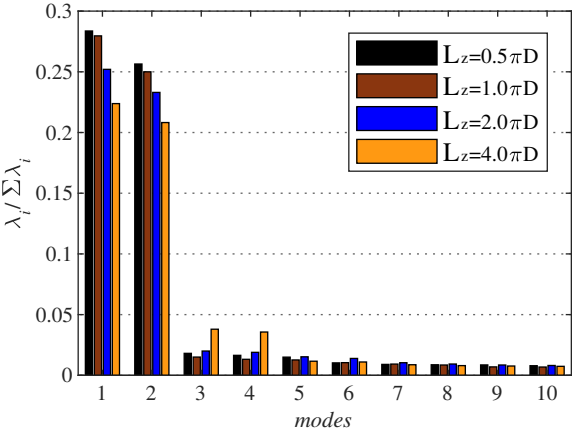


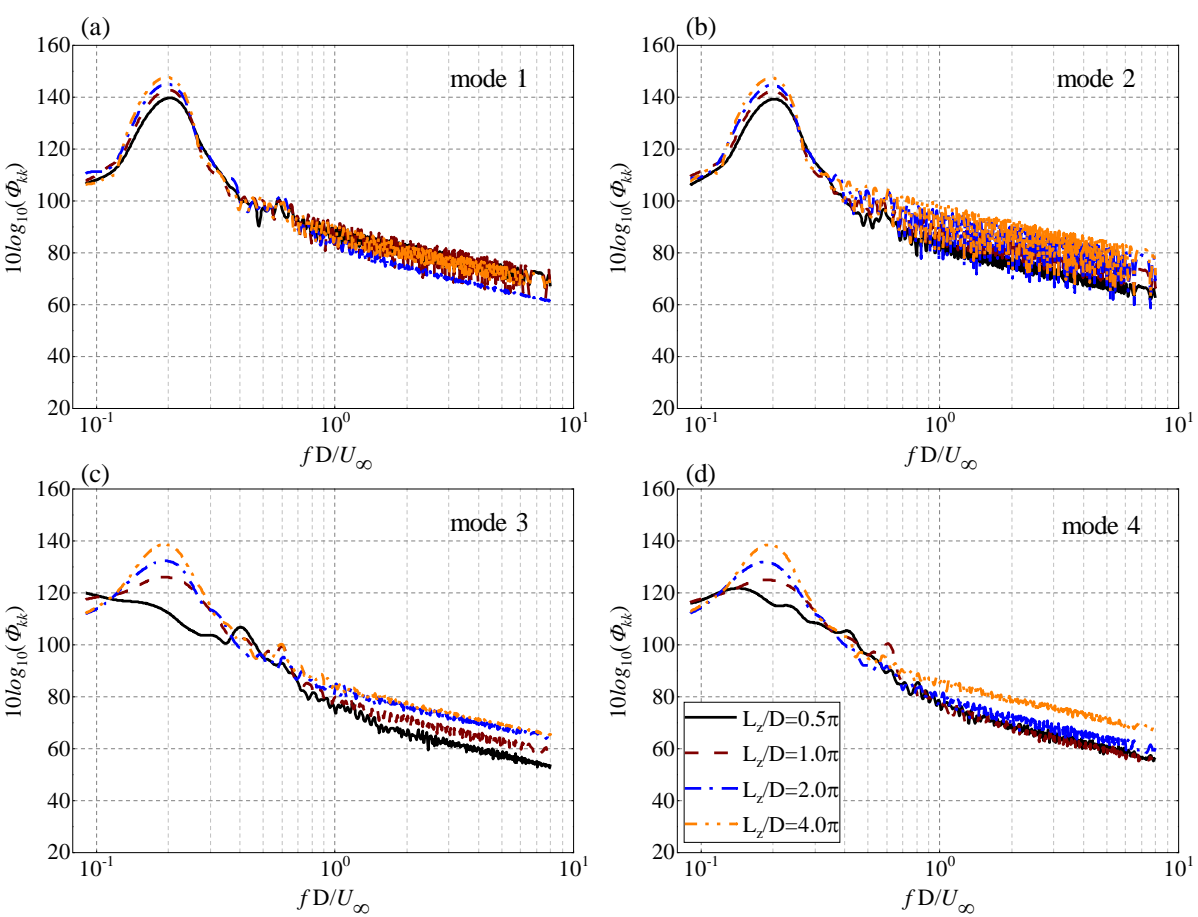


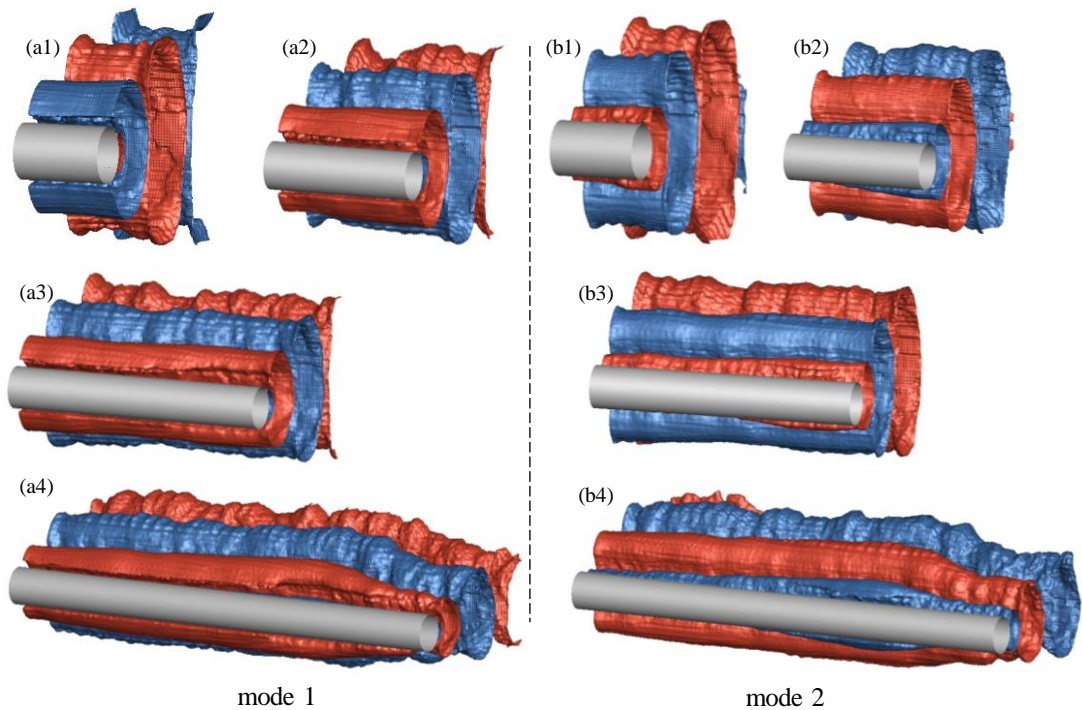
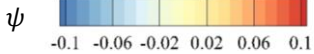




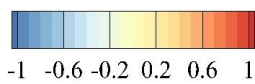




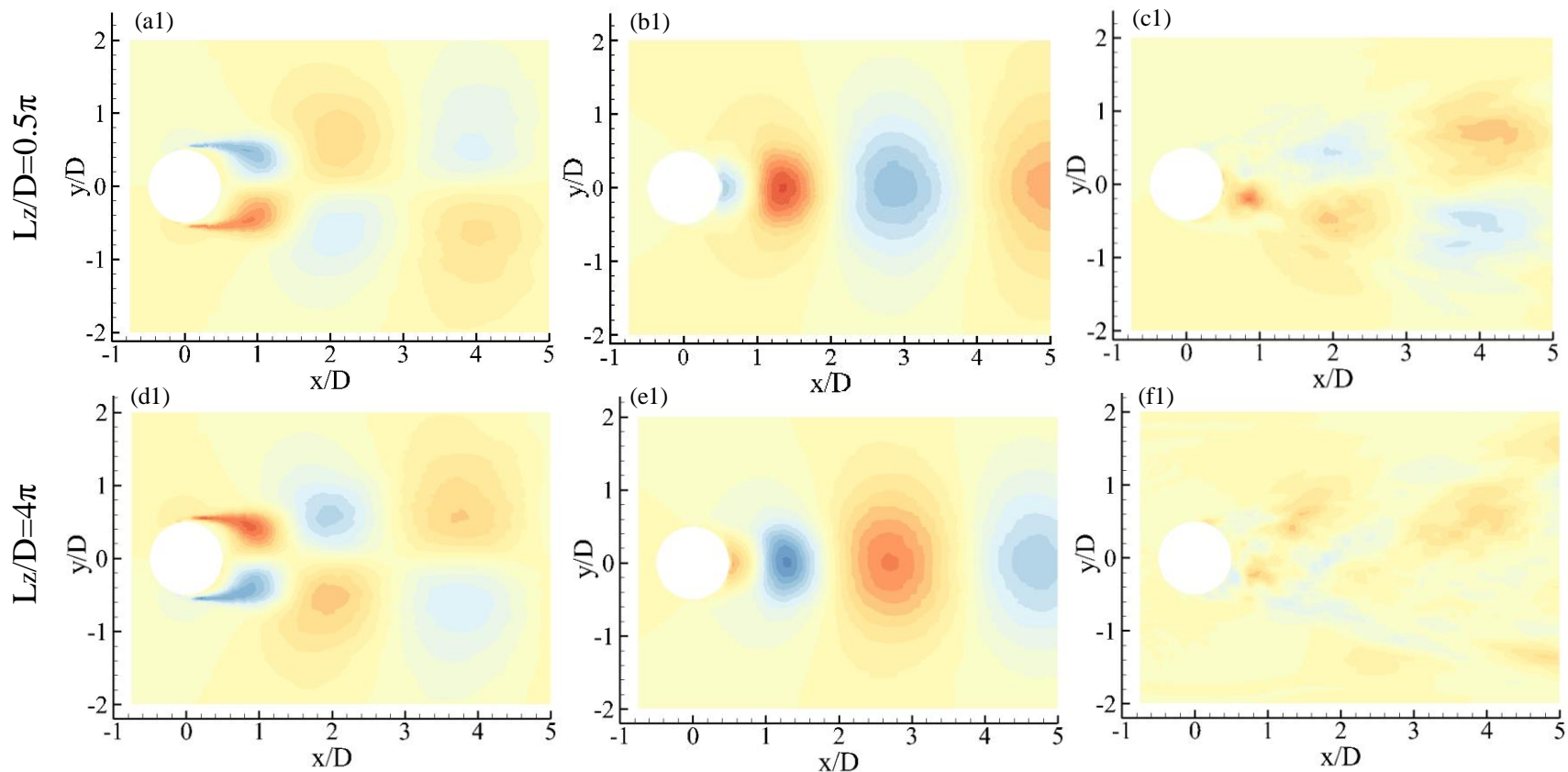




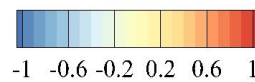
mode 1  $\psi_1$



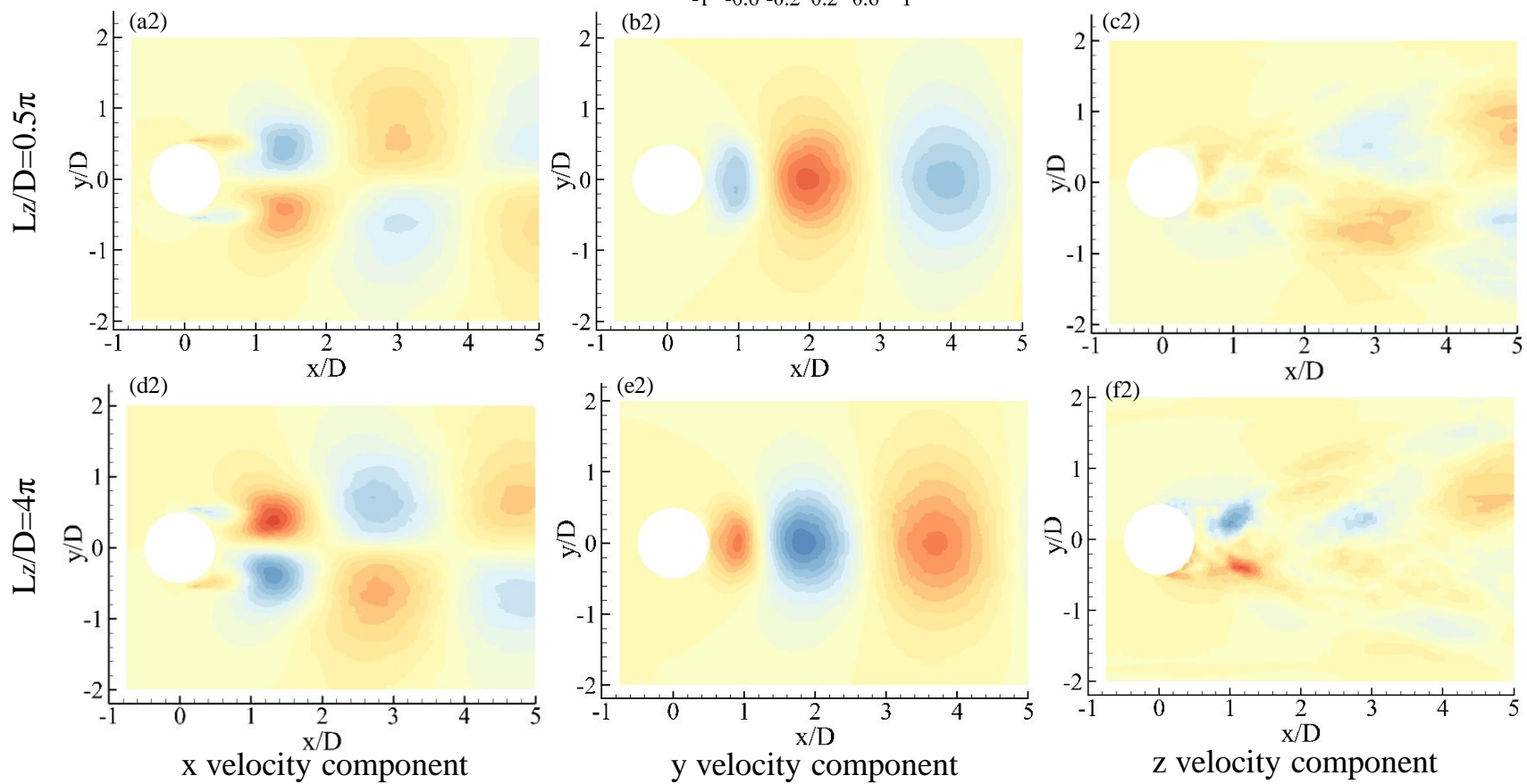
-1 -0.6 -0.2 0.2 0.6 1

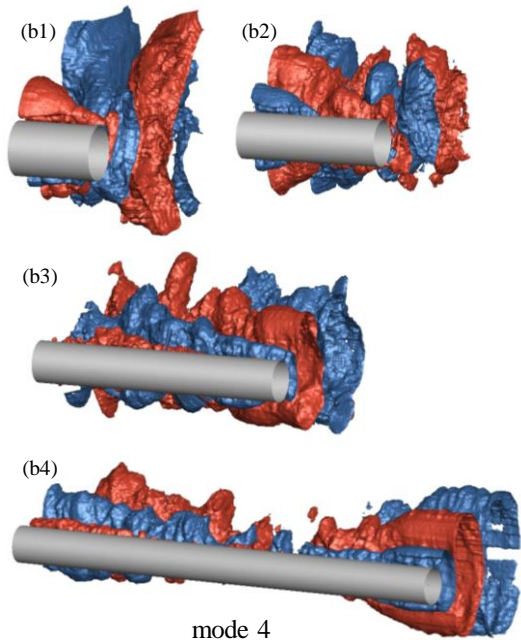
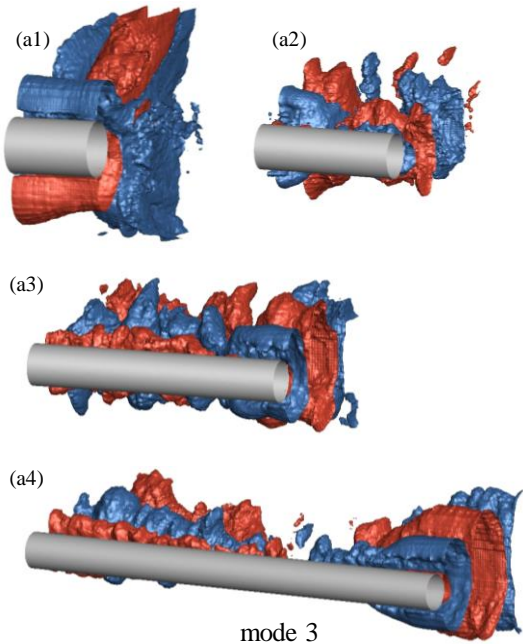
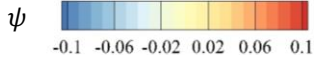


mode 2  $\psi_2$

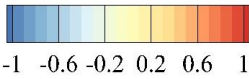


-1 -0.6 -0.2 0.2 0.6 1

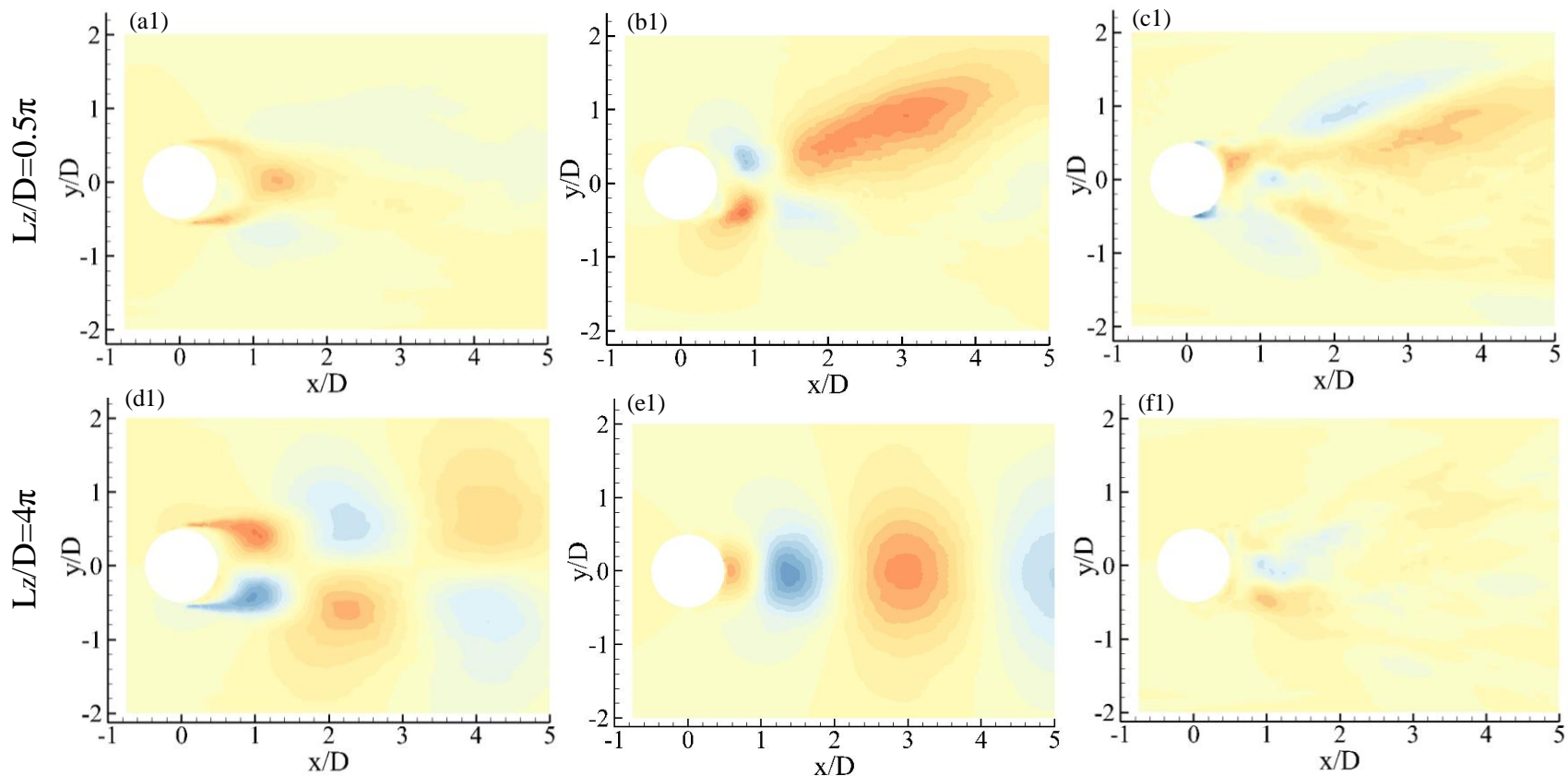




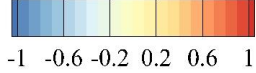
mode 3  $\psi_3$



-1 -0.6 -0.2 0.2 0.6 1



mode 4  $\psi_4$



-1 -0.6 -0.2 0.2 0.6 1

